E-16-W11
#1

Adaptive Control for Flexible Solar Sails

Final Report, 1 April 2003 to 30 November 2007

Research Supported by:
NASA Marshall Space Flight Center, Huntsville, AL
Grant No. NAG8-1292.

Principal Investigator: Dr. Anthony J. Calise*
Co-Principal Investigator: Dr. James I. Craig**
Research Engineer: Dr. Bong-Jun Yang+
Technical Advisor: Dr. Mark S. Whorton, NASA Marshall Space Flight Center

Georgia Institute of Technology
School of Aerospace Engineering
Atlanta, GA 30332-0150

* Professor, (404)894-7145, anthony.calise@ae.gatech.edu
** Professor, (404)894-3042, james.craig@ae.gatech.edu
+ Research Engineer II, (404)385-4940, jun.yang@ae.gatech.edu

Contents

Abstract

A solar sail is an example of a gossamer structure that is proposed as an propulsion system for future space missions. In this report, neural network-based adaptive control is considered for addressing flexibilities in solar sailcrafts.

First, since a solar sail is a large scale flexible structure that requires a long time for its deployment, active control may be required to prevent it from deviating into a non-recoverable state. We conceptually address control of an evolving flexible structure using a growing double pendulum model. Controlling an evolving system poses a major challenge to control design because it involves time-varying parameters, such as inertia and stiffness. By employing a neural network based adaptive control, we illustrate that the evolving double pendulum can be effectively regulated when fixed-gain controllers are deficient due to presence of time-varying parameters.

Second, Neural network-based adaptive control is considered for active control of a highly flexible truss structure which may be used to support solar sail membranes. The objective is to suppress unwanted vibrations in SAFE (Solar Array Flight Experiment) boom, a test-bed located at NASA. Compared to previous tests that restrained truss structures in planar motion, full three dimensional motions are tested. Experimental results illustrate the potential of adaptive control in compensating for nonlinear actuation and modeling error, and in rejecting external disturbances.

Section 1

Introduction

A solar sail is an example of a gossamer structure that has been proposed as a cost effective source of space propulsion for a variety of future space exploration missions. Solar sailcraft gain momentum from reflected photons, and the continuous sunlight pressure provides sufficient propulsive energy for space missions that otherwise are only possible with conventional rocket systems using significant amounts of propellant[1]. Currently, solar sail technology is being developed by the In-Space Propulsion Technology Program managed by NASA's Science Mission Directorate and implemented by the In-Space Propulsion Technology Project at Glenn Research Center. The program's objective is to develop in-space propulsion technologies that enable NASA space science missions by significantly reducing cost, mass and travel times.

In general, the momentum transferred by a single photon is extremely small, and solar sails need to span a very large area to capture and reflect photons in order to achieve a sufficient propulsive force. As a result, useful missions are only possible by use of ultra-lightweight sail films, lightweight deployable booms, and miniature avionics hardware. This makes solar sail structures unique in their constraints on mass, strength and stiffness[2]. From the perspective of maneuvering/steering, solar sailcraft are large gossamer structures that tightly couple attitude and structural dynamics to achieve thrust vector control. The vehicle attitude determines the orientation of the reflective sail surface with respect to the sun and hence determines the direction of the resultant thrust vector. Structural dynamics may impact the thrust vector accuracy by inducing a jitter in the reflected solar radiation and hence affecting direction and magnitude of the thrust vector. In addition, bending vibrations of the booms and sail membranes may limit or adversely affect the stability and performance of the attitude control system.

Depending on imposed assumptions regarding the flexibility of solar sailcraft, various hardware designs and control algorithms for solar sailcraft attitude dynamics have been proposed in the literature. In [3, 4, 5], various hardware configurations and corresponding attitude control systems are investigated in relation to mission trajectories and orbits, with a significant uncertainty being solar radiation pressure disturbance caused by an uncertain offset between the center-of-mass and the center-of-pressure. In those methods, the problem of flexibility is avoided by assuming that the slow maneuvering required for low-thrust propulsion of solar sailcraft still makes a low bandwidth attitude control system look "fast" in relative time-scales[2]. In [6], a solar sailcraft is modeled as a linear flexible 6 degree-of-freedom spacecraft, and different attitude control techniques are compared in the presence of parametric uncertainties. Ref. [7] considers flexibility and its influence on control effectiveness using idealized two-dimensional models. A distributed parameter model for a flexible solar sailcraft is idealized as a rotating central hub with two opposing flexible booms, and linear feedback torque control is applied at the central

hub. Another problem involves control of the solar sail film which involves control of both the dynamics of an ultra-flexible structure and the prevention/elimination of wrinkles. For this purpose distributed actuation and sensing inside the membrane of the gossamer structure have been investigated[8, 9, 10].

In the development of an appropriate control method, major challenges are associated with the uncertainties inherent in flexible solar sails because a comprehensive test for structural analysis is not possible in ground tests due to gravity on Earth. Even when the vacuum and thermal conditions of the space environment are well simulated, solar sail tests must employ awkward gravity offload systems to mitigate the effects of gravity[11]. Further uncertainties in the material properties, test conditions, and modelling errors make it extremely difficult to obtain accurate flexibility characteristics of a flexible solar sail. Therefore, it is highly desirable for a control system to be able to adapt and compensate for system uncertainties.

A neural network (NN) is employed to approximately cancel the uncertainty. It is well established that a NN can approximate any continuous function to any desired accuracy on a bounded set[12], and this has been one of the main reasons given for using a NN in adaptive control approaches[13, 14, 15]. In an output feedback setting, a method that uses a memory unit of input/output delays to approximate an uncertainty has been proposed[16] and shown to be effective in output feedback applications[17, 18, 19, 20].

The adaptive method employed in this report is essentially the decentralized control in [21]. The main difficulty in designing a centralized controller for a distributed control system is that most conventional methods require information from all subsystems for achieving the desired control objective, and the design of a concurrent controller processing a distributed set of sensors and actuators is a formidable task due to its high dimensional complexity. Moreover, if the system to be controlled is uncertain, the design of a single controller for a high dimensional system becomes less feasible in most control systems.

The report is organized as follows. In Section 3, we conceptually consider adaptive control for flexibilities in a solar sail, both during and after deployment. In avoid to excessive complexities associated with modeling the dynamics of a solar sail, we consider a growing double pendulum, which is to mimic a single boom that supports the solar sail membrane. We show that the NN-based decentralized architecture is well suited for evolving system dynamics and stabilize the deploying structure effectively. In Section 3 we apply the NN-based adaptive method to control of a large space structure, the SAFE boom. The objective is suppress unwanted vibrations in the boom, and experimental results illustrate a great potential of the adaptive approach for a highly uncertain flexible structure in which conventional PID controllers are very difficult to design. Future research direction is presented in Section 4.

Section 2

Adaptive Control of Evolving Double Pendulum

In this section, we conceptually address the problem of flexibility arising in solar sails from a perspective that is quite different from typical considerations for flexibility as in [2, 6, 7]. Prior to the commencement of a solar sail mission, the packaged sail must be deployed into its operational configuration. Maintaining stable attitude dynamics of the sailcraft/bus system will be a challenge due to the enormous increase in sailcraft inertia as the support structure and membranes deploy. Therefore, from the perspective of modelling , a simple system-level deployment dynamics for the whole sailcraft is developed in order to assess the deployment behavior for a range of normal and abnormal conditions in [22]. From the perspective of control system design, growing structures induce their own challenges due to time-varying parameters as well as those typical for fully developed flexible systems. In design for an appropriate control method, major challenges are associated with the uncertainties inherent in flexible solar sails because a comprehensive test for structural analysis is not possible in ground tests due to gravity on Earth. Even when the vacuum and thermal conditions of the space environment are well simulated, solar sail tests should employ a gravity-offload system to mitigate the effects of gravity[11]. Further uncertainties in the material properties, test conditions, and modelling errors make it extremely difficult to obtain accurate flexibility characteristics of a flexible solar sail. Therefore, it is highly desirable for a control system to be able to adapt and compensate for system uncertainties.

NN-based adaptive control is considered to address the flexibilities, both during and after deployment, in the presence of parametric and dynamic uncertainties for control of attitude of a solar sail by suppressing unwanted vibrations. In order to avoid excessive complexities related to the modelling of a deploying flexible solar sail, we consider a growing single boom that supports the solar sail membrane and further simplify it as a double pendulum. Two masses evolve into its final configuration, mimicking the growth of the supporting boom of the structure, and we address how NN-based control system adapts to those adversary uncertainties during and after deployment. For further simplicity, the central hub from which the sail boom emerges is assumed fixed.

A critical feature that distinguishes evolving systems from the systems considered in the literature is time-varying parameters. In case of the double pendulum model, lengths and stiffness of the links are time-varying as the inertia of the pendulum evolves. A conventional approach for this case is to schedule gains by introducing a scheduling parameter. However, in our study, the time growth rate for the link is assumed unknown, and there is no way to determine when and how to set gains for controllers. Moreover, the control effectiveness slowly diminishes as the inertia of the system increases,

and leads to gradual degradation for a fixed-gain controller. These challenges suggest that an adaptive approach may be the only viable solution for the evolving double pendulum. However, conventional adaptive approaches[23, 24] allow for only linearly parameterized uncertainties and therefore are not well suited for this application.

Following the methodology in [25, 19], we assume that a nominal controller is already designed independently for each pendulum to maintain its angular position during deployment without any knowledge of flexibility characteristics and couplings that exits between the pendulums. That is, two nominal controllers are designed in a decoupled manner in which each subsystem is assumed independent from each other to avoid the complexity in designing a single controller for the coupled system of dynamics. Since the nominal controllers are intended to control only the local dynamics, without communication with each other, the overall design is equivalent to the decentralized approach described in [21].

2.1 System Dynamics

Consider a single evolving boom consisting of two segments depicted in Figure 2.1, which represents a boom being deployed from the central hub. The nodes n_1, n_2, and n_3 represent the connecting point between the central hub and the first segment, the connecting point between two segments, and the tip of the boom, respectively. The terms t_1 and t_2 are the instants when the first segment and the second segment are fully deployed and are generally unknown in case anomalies arise during deployment. With

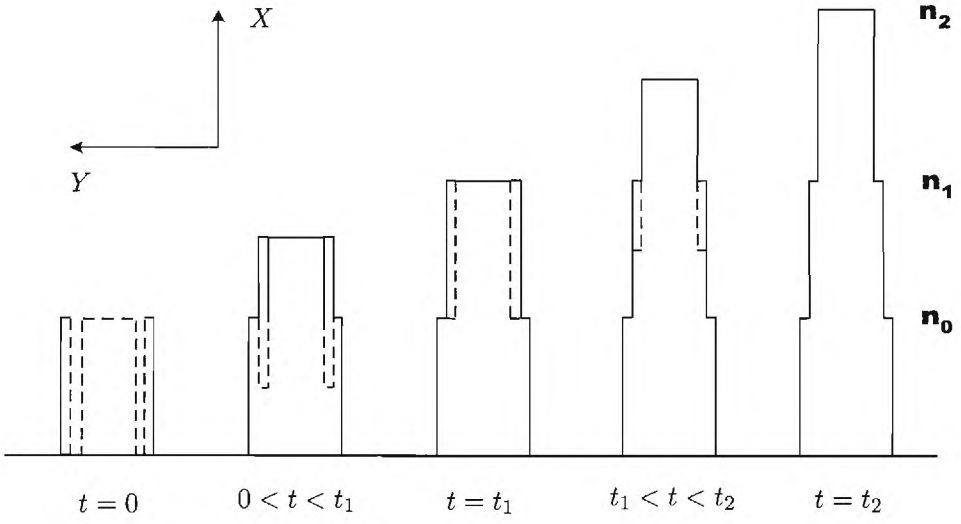

Figure 2.1: Time behavior for an evolving beam

regard to the evolving dynamics in Figure 2.1, we assume the following:

- The segment of the boom continuously evolves.
- Sensors and actuators are collocated at nodes n_0 and n_1.
- The length of each segment is relatively short and treated as an rigid link.

Under the above assumptions, the system depicted in Figure 2.2 is considered as an analogy for the evolving boom for our study, in which the evolving pendulums represent varying inertia distribution. Figure 2.3 depicts possible sources for forces and torques in the configuration when the second pendulum in under deployment. The terms $K_1(t)$ and $K_2(t)$ are stiffness coefficients for torsional springs, which are introduced to model the flexibility of the boom. As seen in Figure 2.1, torsional stiffness is expected to depend on the length of the segment that is not deployed and therefore is modelled as time-varying parameters. The damping terms D_1 and D_2 are assumed constant. The terms $F_{a_i}(t)$ and $F_{b_i}(t)$ $(i = x, y)$ are external forces that are applied directly to the masses m_1 and m_2. The terms $u_1(t)$ and $u_2(t)$ are control torques provided by control systems. The effect of the sun light is detailed in the subsequent equation motion. Referring to Figures 2.2 and 2.3, the equation of motion for the evolving system is

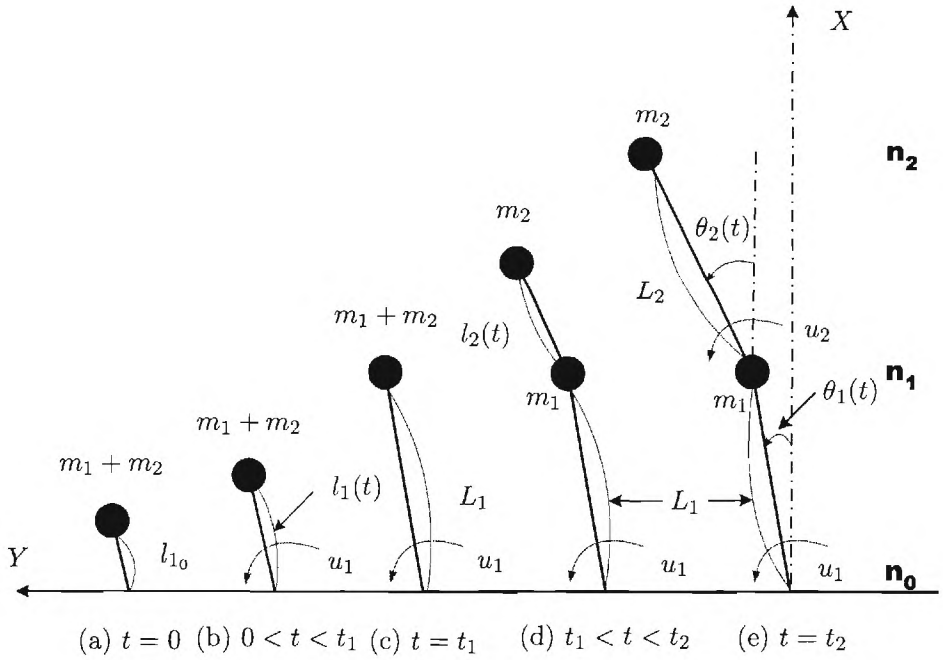

Figure 2.2: Time behavior for evolving pendulums

derived as follows.

2.1.1 When the first pendulum evolves $(0 \leq t \leq t_1)$

We assume that the pendulum length increases in a constant rate, and the length of the first pendulum is determined by

$$l_1(t) = l_{1_0} + \beta_l t, \tag{2.1}$$

where l_{1_0} is the initial length for the mass m_1, and β_l is the increase rate for the pendulum. The stiffness, however, decreases as the pendulum evolves and is described by

$$K_1(t) = K_{1_0} - \alpha_{K_1} t, \tag{2.2}$$

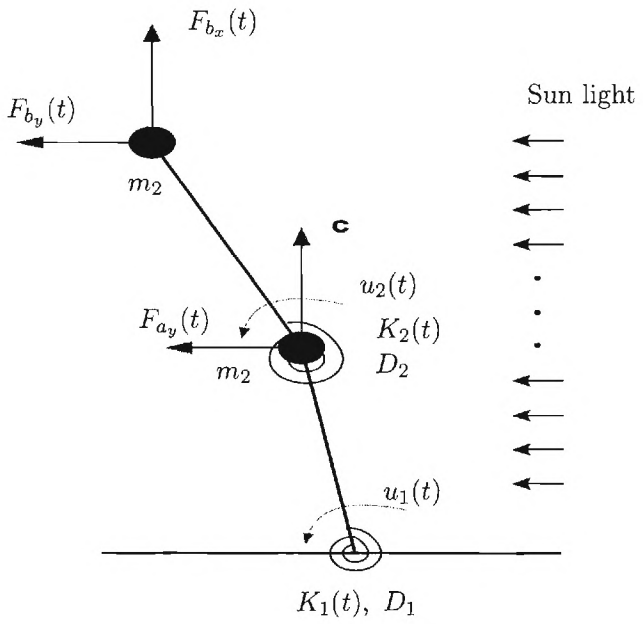

Figure 2.3: External forces while the second pendulum deploys

where K_{1_0} is an initial stiffness constant, and α_{K_1} is the decrease rate for the stiffness. The resulting equation of motion is

$$\begin{aligned} &M_1(l_1(t),\theta_1)\ddot{\theta}_1 + D_1\dot{\theta}_1 + K_1(t)\theta_1 + f_{n_1}(l_1(t),\dot{\theta}_1,\theta_1) \\ &= u_1(t) + f_{d_1}(l_1(t),\theta_1) + f_{s_1}(l_1(t),\theta_1), \end{aligned} \tag{2.3}$$

where $M_1(l_1(t),\theta_1) = (m_1+m_2)l_1(t)^2$, D_1 is a damping coefficient, $f_{n_1}(l_1(t),\dot{\theta}_1),\theta_1)$ represents nonlinear terms due to Coriolis effect; $f_{n_1}(\dot{\theta}_1,\theta_1) = 2(m_1+m_2)l_1(t)\dot{l}_1\dot{\theta}_1 = 2(m_1+m_2)\beta_l l_1(t)\dot{\theta}_1$, $f_{d_1}(\theta_1) = -l_1(t)\sin\theta_1 F_{a_x}(t) + l_1(t)\cos\theta_1 F_{a_y}(t)$, and $F_{s_1}(l_1(t),\theta_1)$ is the torque caused by the solar pressure. Following Ref.[?], we model it as

$$f_{s_1}(l_1(t),\theta_1) = \frac{1}{2}\rho_s l_1(t)^2\cos\theta_1, \tag{2.4}$$

where ρ_s is the solar force applied at a unit length when the sunlight is perpendicular to the pendulum.

2.1.2 When the second pendulum evolves ($t_1 < t \leq t_2$)

For this period, the first pendulum is fully deployed, i.e., $l_1(t) = l_{1_0} + \beta_l t_1 = L_1$, and $\dot{l}_1(t) = 0$. Similarly, $K_1(t) = K_{1_0} - \alpha_{K_1} t_1 = K_{1_f}$. However, the second pendulum is evolving, so we have

$$l_2(t) = l_{2_0} + \beta_l(t-t_1),\ K_2(t) = K_{2_0} - \alpha_{K_2}(t-t_1). \tag{2.5}$$

The equation of motion is then derived as

$$\begin{aligned} &M(l_2(t),\boldsymbol{\theta})\ddot{\boldsymbol{\theta}} + D\dot{\boldsymbol{\theta}} + K(t)\boldsymbol{\theta} + \boldsymbol{f}_n(l_2(t),\dot{\boldsymbol{\theta}},\boldsymbol{\theta}) \\ &= B_u\boldsymbol{u} + \boldsymbol{f}_s(l_2(t),\boldsymbol{\theta}) + B_a(\theta_1)\boldsymbol{F}_a + B_b(l_2(t),\boldsymbol{\theta})\boldsymbol{F}_b, \end{aligned} \tag{2.6}$$

where

$$\boldsymbol{\theta} = \begin{bmatrix} \theta_1 \\ \theta_2 \end{bmatrix}, \ \boldsymbol{u} = \begin{bmatrix} u_1 \\ u_2 \end{bmatrix}, \ \boldsymbol{F}_a = \begin{bmatrix} F_{a_x} \\ F_{a_y} \end{bmatrix}, \ \boldsymbol{F}_b = \begin{bmatrix} F_{b_x} \\ F_{b_y} \end{bmatrix},$$

and

$$M(l_2(t), \boldsymbol{\theta}) = \begin{bmatrix} (m_1+m_2)L_1^2 & m_2 L_1 l_2(t)\cos(\theta_2-\theta_1) \\ m_2 L_1 l_2(t)\cos(\theta_2-\theta_1) & m_2 l_2(t)^2 \end{bmatrix}, D = \begin{bmatrix} D_1+D_2 & -D_2 \\ -D_2 & D_2 \end{bmatrix},$$

$$K(t) = \begin{bmatrix} K_{1_f}+K_2(t) & -K_2(t) \\ -K_2(t) & K_2(t) \end{bmatrix}, B_u = \begin{bmatrix} 1 & 0 \\ 0 & 1 \end{bmatrix}, B_a(\theta_1) = \begin{bmatrix} -L_1\sin\theta_1 & L_1\cos\theta_1 \\ 0 & 0 \end{bmatrix},$$

$$B_b(l_2(t), \boldsymbol{\theta}) = \begin{bmatrix} -L_1\sin\theta_1 & L_1\cos\theta_1 \\ -l_2(t)\sin\theta_2 & l_2(t)\cos\theta_2 \end{bmatrix}. \tag{2.7}$$

The term $\boldsymbol{f}_n(l_2(t), \dot{\boldsymbol{\theta}}, \boldsymbol{\theta})$ are due to Coriolis effects and centrifugal terms and are given by

$$\boldsymbol{f}_n(l_2(t), \dot{\boldsymbol{\theta}}, \boldsymbol{\theta}) = \begin{bmatrix} 2m_2 L_1 \dot{l}_2(t)\dot{\theta}_2\cos(\theta_2-\theta_1) - m_2 L_1 l_2(t)\dot{\theta}_2^2\sin(\theta_2-\theta_1) \\ 2m_2 l_2(t)\dot{l}_2(t)\dot{\theta}_2 + m_2 L_1 l_2(t)\dot{\theta}_1^2\sin(\theta_2-\theta_1) \end{bmatrix}, \tag{2.8}$$

and the solar torque $\boldsymbol{f}_s(l_2(t), \boldsymbol{\theta})$ is given by

$$\boldsymbol{f}_s(l_2(t), \boldsymbol{\theta}) = \begin{bmatrix} \frac{1}{2}\rho_s L_1^2\cos\theta_1 + \rho_s L_1 l_2(t)\cos\theta_2\cos(\theta_2-\theta_1) \\ \frac{1}{2}\rho_s l_2(t)^2\cos\theta_2 \end{bmatrix}. \tag{2.9}$$

At the beginning of evolution, the second pendulum has the same angle as the first pendulum because they move together for $0 < t < t_1$, and the initial conditions for the second pendulum are set as $\theta_2(t_1) = \theta_1(t_1)$ and $\dot{\theta}_2(t_1) = \dot{\theta}_1(t_1)$.

2.1.3 After full deployment ($t > t_2$)

After the pendulums are fully deployed, $l_2(t) = l_{2_0} + \beta_l(t_2 - t_1) = L_2$ and $K_2 = K_{2_0} - \alpha_{K_2}(t_2 - t_1) = K_{2_f}$. This leads to

$$\begin{aligned} &M(\boldsymbol{\theta})\ddot{\boldsymbol{\theta}} + D\dot{\boldsymbol{\theta}} + K\boldsymbol{\theta} + \boldsymbol{f}_n(\dot{\boldsymbol{\theta}}, \boldsymbol{\theta}) \\ &= B_u\boldsymbol{u} + \boldsymbol{f}_s(\boldsymbol{\theta}) + B_a(\theta_1)\boldsymbol{F}_a + B_b(\boldsymbol{\theta})\boldsymbol{F}_b, \end{aligned} \tag{2.10}$$

where each terms are determined from (2.7)-(2.9) by letting $\dot{l}_2(t) = 0$ and $l_2(t) = L_2$. Note that after the full deployment, the lengths of both pendulums and torsional stiffness terms are constants and $l_2(t)$ term is removed in (2.10).

The parameters used in simulating the evolving beams are

$$\begin{aligned} &m_1 = m_2 = 2\ (m),\ l_{1_0} = l_{2_0} = 1\ (m),\ L_1 = L_2 = 10\ (m),\ t_1 = 50sec.,\ t_2 = 100sec.,\ \beta_l = \frac{L_1 - l_{1_0}}{t_1}(m/s), \\ &K_{1_0} = K_{2_0} = 2\ (N/m),\ K_{1_f} = K_{2_f} = 0.5\ (N/m),\ \alpha_{K_1} = \alpha_{K_2} = \frac{K_{1_0} - K_{1_f}}{t_1}\ (N/s), \\ &D_1 = 0.0001(N\cdot s/m),\ D_2 = 0.0008\ (N\cdot s/m),\ \rho_s = 0.01\ (N/m). \end{aligned} \tag{2.11}$$

The initial conditions are set as $\theta_1(0) = 20^o$, $\dot{\theta}_1(0) = 0$.

2.2 Control Design

2.2.1 Control objective and decentralized architecture

In the deploying double pendulum in Figure 2.2, the control system is also assumed to evolve and is immediately activated when each pendulum starts to evolve. The measurements are angular displacements for each pendulums, i.e., $y_1(t) = \theta_1(t)$ for $0 < t \leq t_1$, and $y_1(t) = \theta_1(t)$, $y_2(t) = \theta_2(t)$ for $t > t_1$, and $u_1(t)$ and $u_2(t)$ are control torques and are available at the same time when the measurements are available. The control objective is to design a control law for u_1 for $0 < t \leq t_1$ and u_1 and u_2 for $t > t_2$ so as to stabilize the pendulum during and after deployment when the deployment rate (therefore, the length of the pendulum during deployment) is not available, which mimics the situation in which proper positioning of the solar sail system is impeded due to anomalies in deploying process.

This objective poses serious challenges in designing a control law for u_1 and u_2. First, system parameters are slowly time-varying with its rate proportional to the unknown rate of evolution. Second, the control effectiveness lessens, as the system evolves, and hence leads to gradual degradation of system performance for a fixed-gain controller. These challenges makes an adaptive approach be a viable solution, and we seek to control the deploying dynamics using the method in [26, 25, 27] that is formulated in a way that augments an fixed-gain linear controller by adding adaptive control. We assume that a lead controller is already designed for each pendulum to maintain its angular position during deployment. They are designed in a decoupled manner, in which θ_1 and θ_2 dynamics are assumed independent from each other, without considering flexibility. In the sense that θ_1 controller and θ_2 controller are in independent control of dynamics without any communication each other, the overall design architecture falls into the decentralized one described in [21]. When we augment the lead controllers using NNs, we also introduce an arbitrary reference model as in [27].

Figure 2.4 lays out the control architecture for the evolving pendulum system. In Figure 2.4(a), the second control system is only active for $t > t_2$ and denoted in blue double dotted line. The θ_1 and θ_2 controllers have the same architecture, and Figure 2.4(b) shows how the θ_1-controller is designed. The block representing the adaptive portion of the design is shaded. Note that applying the same reference command θ_c for both controllers means that the objective of two controllers is to synchronize their motion.

2.2.2 Design of a fixed-gain controller $G_{ec}(s)$

The linear controller is designed considering the following models for m_1 and m_2

$$\begin{aligned} \ddot{\theta}_1 &= b_1 u_1, \ t > 0 \\ \ddot{\theta}_2 &= b_2 u_2, \ t > t_1. \end{aligned} \tag{2.12}$$

The control effectiveness terms are defined as

$$b_1 = \frac{1}{(\hat{m}_1 + \hat{m}_2) l_{1_0}^2}, \ b_2 = \frac{1}{\hat{m}_2 l_{2_0}^2}, \tag{2.13}$$

where $\hat{m}_1 = 1$ and $\hat{m}_2 = 1$ are estimates for m_1 and m_2. Note that the plant model does not consider any flexibility or coupling dynamical effects between two pendulums. Letting

$$u_1 = \frac{1}{b_1}\nu_1, \ u_2 = \frac{1}{b_2}\nu_2 \tag{2.14}$$

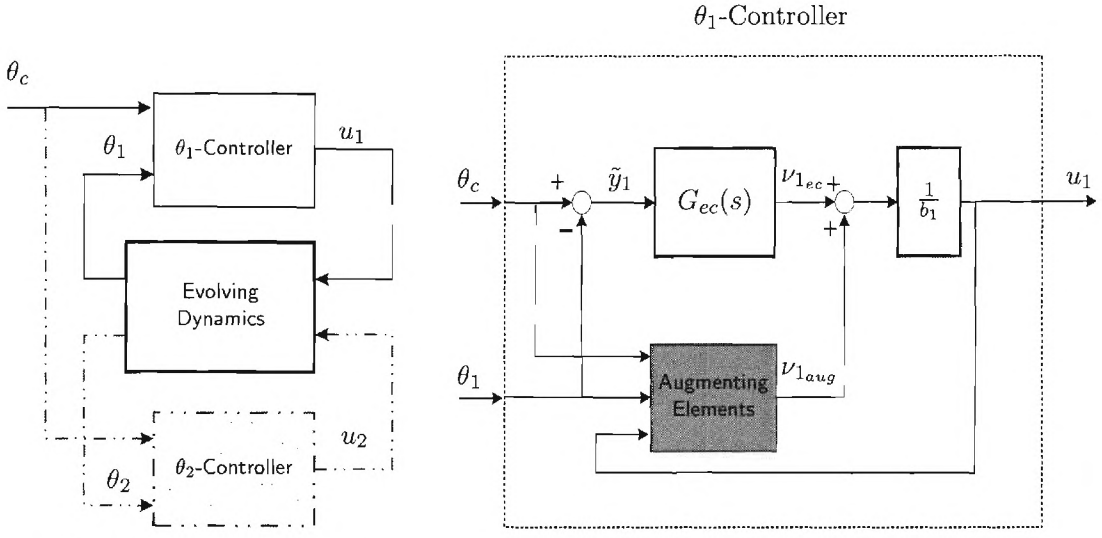

(a) Overall Control Architecture

(b) Inside of θ_1-Controller

Figure 2.4: Control System Architecture

leads to

$$\ddot{\theta}_i = \nu_i, \ i = 1, 2. \tag{2.15}$$

For $G_{ec}(s)$ in Figure 2.4(b), a lead compensator is designed

$$\nu_{i_{ec}} = G_{ec}(s)\tilde{y}_i = K_p\tilde{y}_i + K_d\frac{s}{s/\omega_l + 1}\tilde{y}_i, \tag{2.16}$$

where $\tilde{y}_i = \theta_c - \theta_i$ $(i = 1, 2)$, and $K_p = 0.0163$ $K_d = 3.1442$, and $\omega_l = 20$(rad/s) leads to the closed-loop poles of $-18.8904, -1.1044, -0.0052$ for the systems in (2.12).

With (2.14), compared to the plant model in (2.15), the true system in (2.3) ,(2.6), and (2.10) is described by

$$\begin{aligned} \ddot{\theta}_1 &= \nu_1 + \Delta_1(t), \ t > 0 \\ \ddot{\theta}_2 &= \nu_2 + \Delta_2(t), \ t > t_1, \end{aligned} \tag{2.17}$$

where the modelling error $\Delta_i(t)$ $(i = 1, 2)$ are defined as follows.

- For $0 < t \leq t_1$

$$\begin{aligned} \Delta_1(t) =& \frac{1}{M(l_1(t), \theta_1)}\left[-D_1\dot{\theta}_1 - K_1\theta_1 - f_n(l_1(t), \dot{\theta}_1, \theta_1) + f_{s_1}(l_1(t), \theta_1) + f_d(l_1(t), \theta_1)\right] \\ &+ b_1\left(\frac{(\hat{m}_1 + \hat{m}_2)l_{1_0}^2}{(m_1 + m_2)l_1(t)^2} - 1\right)u_1, \end{aligned} \tag{2.18}$$

  where the control effectiveness term is explicitly given to show its time-varying nature due to increase in the inertia. It is bounded according to the following inequalities

$$b_1\left(\frac{(\hat{m}_1 + \hat{m}_2)}{(m_1 + m_2)} - 1\right) > b_1\left(\frac{(\hat{m}_1 + \hat{m}_2)l_{1_0}^2}{(m_1 + m_2)l_1(t)^2} - 1\right) < b_1\left(\frac{(\hat{m}_1 + \hat{m}_2)l_{1_0}^2}{(m_1 + m_2)L_1^2} - 1\right) > -b_1$$

The choice of b_1 in (2.12) guarantees that

$$|b_1 u_1| > \left| b_1 \left(1 - \frac{(\hat{m}_1 + \hat{m}_2) l_{1_0}^2}{(m_1 + m_2) l_1(t)^2} \right) u_1 \right|$$

whenever $u_1 \neq 0$. The first term in (2.18) tends to decrease, with $\dot{\theta}_1$ and θ_1 fixed, as m_1 evolves except the solar force term

$$\frac{f_{s_1}(l_1(t), \theta_1)}{M(l_1(t), \theta_1)} = \frac{\rho_s \cos\theta_1}{2(m_1 + m_2)}$$

because the inertia term $M(l_1(t), \theta_1)$ is of the second order with respect to the pendulum length $l_1(t)$.

- For $t_1 < t \leq t_2$

  Letting $\boldsymbol{\Delta}(t) = [\Delta_1(t),\ \Delta_2(t)]^\top$, similarly as in (2.18), we have

$$\begin{aligned} \boldsymbol{\Delta}(t) =& M(l_2(t), \boldsymbol{\theta})^{-1} \Big[-D\dot{\boldsymbol{\theta}} - K(t)\boldsymbol{\theta} - \boldsymbol{f}_n(l_2(t), \dot{\boldsymbol{\theta}}, \boldsymbol{\theta}) + \boldsymbol{f}_s(l_2(t), \boldsymbol{\theta}) \\ & + B_a(\theta_1)\boldsymbol{F}_a + B_b(l_2(t), \boldsymbol{\theta})\boldsymbol{F}_b \Big] + \underbrace{\left(M(l_2(t), \boldsymbol{\theta})^{-1} B_u - \hat{B} \right)}_{B_\delta} \boldsymbol{u}, \end{aligned} \tag{2.19}$$

  where $\hat{B} = \text{diag}\{b_1,\ b_2\}$. The expression for the control effectiveness term is

$$B_\delta = \begin{bmatrix} b_1 \left(\frac{(\hat{m}_1+\hat{m}_2) l_{1_0}^2}{(m_1+m_2) L_1^2} \frac{1}{1 - \frac{m_2}{m_1+m_2} \cos^2(\theta_2 - \theta_1)} - 1 \right) & -\frac{1}{(m_1+m_2) L_1^2} \frac{L_1 / l_2(t) \cos(\theta_2 - \theta_1)}{1 - \frac{m_2}{m_1+m_2} \cos^2(\theta_2 - \theta_1)} \\ -\frac{1}{(m_1+m_2) L_1^2} \frac{L_1 / l_2(t) \cos(\theta_2 - \theta_1)}{1 - \frac{m_2}{m_1+m_2} \cos^2(\theta_2 - \theta_1)} & b_2 \left(\frac{\hat{m}_2 l_{2_0}^2}{m_2 l_2(t)^2} \frac{1}{1 - \frac{m_2}{m_1+m_2} \cos^2(\theta_2 - \theta_1)} - 1 \right) \end{bmatrix}.$$

- For $t > t_2$

$$\begin{aligned} \boldsymbol{\Delta}(t) = \boldsymbol{\Delta}(\dot{\boldsymbol{\theta}}, \boldsymbol{\theta}) =& M(\boldsymbol{\theta})^{-1} \Big[-D\dot{\boldsymbol{\theta}} - K\boldsymbol{\theta} - \boldsymbol{f}_n(\dot{\boldsymbol{\theta}}, \boldsymbol{\theta}) + \boldsymbol{f}_s(\boldsymbol{\theta}) \\ & + B_a(\theta_1)\boldsymbol{F}_a + B_b(\boldsymbol{\theta})\boldsymbol{F}_b \Big] + \left(M(\boldsymbol{\theta})^{-1} B_u - \hat{B} \right) \boldsymbol{u}. \end{aligned} \tag{2.20}$$

2.2.3 Augmenting elements

The augmenting approaches in [26, 25] define a reference model, which determines the best possible performance, which is made up of the plant regulated by the existing control system. This leads to having a reference model whose order equals the order of the plant model plus the order of the controller. For complex systems, this can be excessively high. As an alternative, we can employ an arbitrarily chosen reference model that has the same relative degree of the plant[27].

Following the rationale in [27], we introduce a second order reference model described by

$$\ddot{\theta}_r = -2\zeta_r \omega_r \dot{\theta}_r + \omega_r^2 \theta_r + \omega_r^2 \theta_c, \tag{2.21}$$

where $\zeta_r = 0.9$, $\omega_r = 1$ (rad/s), for both θ_1 and θ_2 dynamics. Since the augmenting elements in Figure 2.4(b) are exactly the same, we use the subscript i to denote both 1 and 2. As seen in Figure 2.4(b), let

$$\nu_i = \nu_{i_{ec}} + \nu_{i_{aug}}. \tag{2.22}$$

By defining the tracking error as

$$e_i = \theta_r - \theta_i, \tag{2.23}$$

comparing (2.17) to (2.21) leads to

$$\ddot{e}_i = \ddot{\theta}_r - \nu_{i_{aug}} + \Delta_i'(t), \tag{2.24}$$

where

$$\Delta_i'(t) = \Delta_i(t) - \nu_{i_{ec}}. \tag{2.25}$$

By letting

$$\nu_{i_{aug}} = \ddot{\theta}_r + \nu_{i_{dc}} - \nu_{i_{ad}}, \tag{2.26}$$

we have

$$\ddot{e}_i = -\nu_{i_{dc}} + \nu_{i_{ad}} - \Delta_i'(t), \tag{2.27}$$

which is exactly the same as the one in [28, 29] and hereafter we follow the design method in [28, 29]. The compensator $\nu_{i_{dc}}$ is designed to stabilize the dynamics in (2.27) when $\nu_{i_{ad}} - \Delta_i'(t) = 0$, and $\nu_{i_{ad}}$ is an adaptive signal that approximates for the uncertainty $\Delta_i'(t)$.

With the definition

$$\boldsymbol{e}_i = \begin{bmatrix} e_i & \dot{e}_i \end{bmatrix}^\top = \begin{bmatrix} e_{i_1} & \dot{e}_{i_2} \end{bmatrix}^\top, \tag{2.28}$$

the error dynamics in (2.27) can be written in the following state space form

$$\begin{aligned} \dot{\boldsymbol{e}}_i =& A\boldsymbol{e}_i + \boldsymbol{b}(-\nu_{i_{dc}} + \nu_{i_{ad}} - \Delta_i') \\ e_i =& \boldsymbol{c}^\top \boldsymbol{e}_i, \end{aligned} \tag{2.29}$$

where

$$A = \begin{bmatrix} 0 & 1 \\ 0 & 0 \end{bmatrix}, \ \boldsymbol{b} = \begin{bmatrix} 0 \\ 1 \end{bmatrix}, \ \boldsymbol{c}^\top = \begin{bmatrix} 1 \\ 0 \end{bmatrix}. \tag{2.30}$$

The compensator $\nu_{i_{dc}}$ is designed similarly as in (2.16)

$$\nu_{i_{dc}} = K_{dc_p} e_i + K_{dc_d} \hat{e}_{i_2}, \tag{2.31}$$

where $K_{dc_p} = 0.1$, $K_{dc_d} = 0.2$, and $\hat{e}_{i_2}$ is obtained by

$$\hat{e}_{i_2} = \frac{s}{s/\omega_l + 1} e_i. \tag{2.32}$$

The compensator is written in state space form as

$$\begin{aligned} \dot{x}_{dc} =& a_c x_{dc} + b_c e_i \\ \nu_{i_{dc}} =& c_c x_{dc} + d_c e_i, \end{aligned} \tag{2.33}$$

and results in the following closed-loop error dynamics

$$\dot{\boldsymbol{E}} = \bar{A}\boldsymbol{E} + \bar{\boldsymbol{b}}(\nu_{i_{ad}} - \Delta_i'), \tag{2.34}$$

whose poles are located at $-19.80, -0.10 \pm 0.3j$, and

$$\boldsymbol{E} = \begin{bmatrix} \boldsymbol{e}_i \\ x_{dc} \end{bmatrix}, \ \bar{A} = \begin{bmatrix} A - \boldsymbol{b} d_c c_c & -\boldsymbol{b} c_c \\ b_c \boldsymbol{c}^\top & a_c \end{bmatrix}, \ \bar{\boldsymbol{b}} = \begin{bmatrix} \boldsymbol{b} \\ 0 \end{bmatrix}. \tag{2.35}$$

Since $\bar{A}$ is Hurwitz, for any $Q > 0$, there exists a $P > 0$ such that

$$\bar{A}P + P\bar{A} + Q = 0. \tag{2.36}$$

In simulation Q is set as $I_{3\times 3}$.The adaptive signal $\nu_{i_{ad}}$ is implemented using a NN, and the overall augmenting elements are depicted in Figure 2.5.

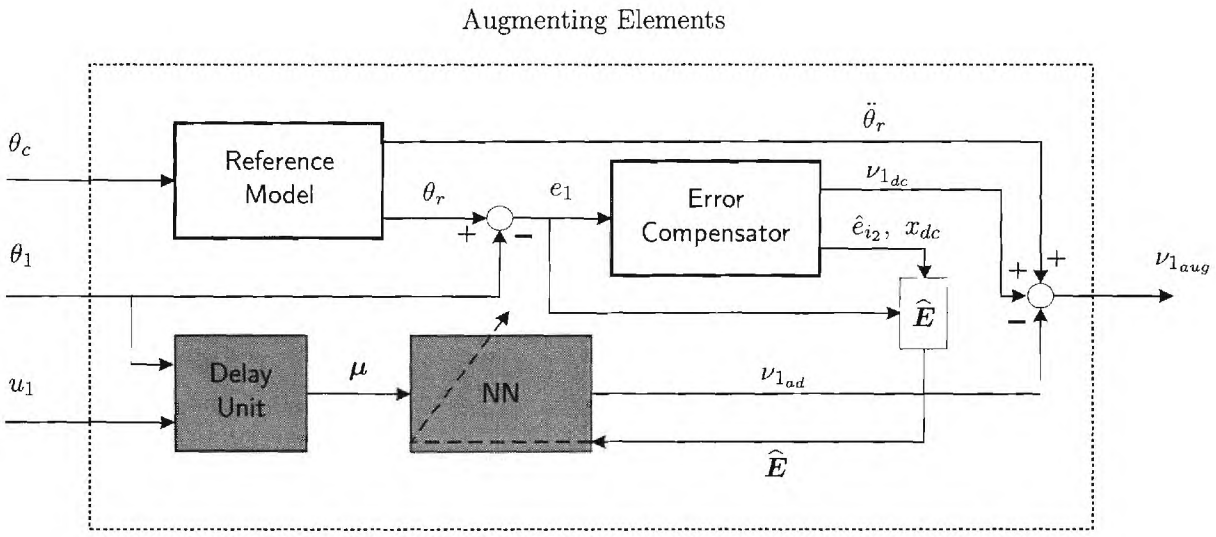

Figure 2.5: Diagram for augmenting elements

2.2.4 Adaptive element

A single hidden-layer NN (SHLNN) is used to approximate $\Delta_i'(t)$ in (2.25) using a memory unit of sampled input/output pairs. With t fixed, there exist bounded constant weights, $W(t), V(t)$, such that:

$$\Delta_i'(t) = \boldsymbol{W}(t)^\top \boldsymbol{\sigma}(V(t)^\top \boldsymbol{\mu}) + \varepsilon(\boldsymbol{\mu}),\ |\varepsilon(\boldsymbol{\mu})| \leq \epsilon^*, \tag{2.37}$$

where $\varepsilon(\boldsymbol{\mu})$ is the NN reconstruction error, which is upper bounded by ϵ^* on a compact domain of interest, and $\boldsymbol{\mu}$ is the network input vector

$$\begin{aligned} \boldsymbol{\mu}(t) &= [\ 1 \quad \bar{\boldsymbol{u}}_d^T(t) \quad \bar{\boldsymbol{y}}_d^T(t)\ ]^T \\ \bar{\boldsymbol{u}}_d^T(t) &= [u_i(t) \quad u_i(t-d) \quad \cdots u_i(t-(n_1-r-1)d)]^T \\ \bar{\boldsymbol{y}}_d^T(t) &= [y_i(t) \quad y_i(t-d) \cdots y_i(t-(n_1-1)d)]^T \end{aligned} \tag{2.38}$$

in which n_1 is the length of the window and is generally required to be greater than or equal to the system dimension, $d > 0$ is a time-delay, r is the relative degree of the output, $\boldsymbol{\sigma}$ is a vector of squashing functions, $\sigma(\cdot)$, whose i^{th} element is defined as $\left[\boldsymbol{\sigma}(V^\top \boldsymbol{\mu})\right]_i = \sigma\left[(V^\top \boldsymbol{\mu})_i\right]$, and $y_i(t)$ is an output of the system, i.e., $y_i(t) = \theta_i(t)$. Notice that $W_i(t)$ and $V_i(t)$ are time-varying due to the time-varying parameters $l_i(t)$ and $K_i(t)$. We assume that the varying rate for those parameters is much more smaller than the bandwidth of the controller we design, and those parameters can be treated as constants for some time period $[t-\delta, t+\delta]$, $\delta > 0$. In other words, from the control design perspective, the ideal weights $\boldsymbol{W}(t)$ and $V(t)$ are assumed constants because they vary much more slowly than the NN weights. The squashing functions are chosen as sigmoidal functions

$$[\boldsymbol{\sigma}(V(t)^\top \boldsymbol{\mu})]_i = \frac{1}{1 + e^{-a(V(t)^\top \boldsymbol{\mu})_i}},\ i = 1, \ldots, N, \tag{2.39}$$

where $a = 1$ represents the activation potential, and N is the number of neurons in the hidden layer.

The adaptive signal $\nu_{i_{ad}}$ is designed as

$$\nu_{i_{ad}} = \widehat{\boldsymbol{W}}(t)^\top \boldsymbol{\sigma}(\widehat{V}(t)^\top \boldsymbol{\eta}) \tag{2.40}$$

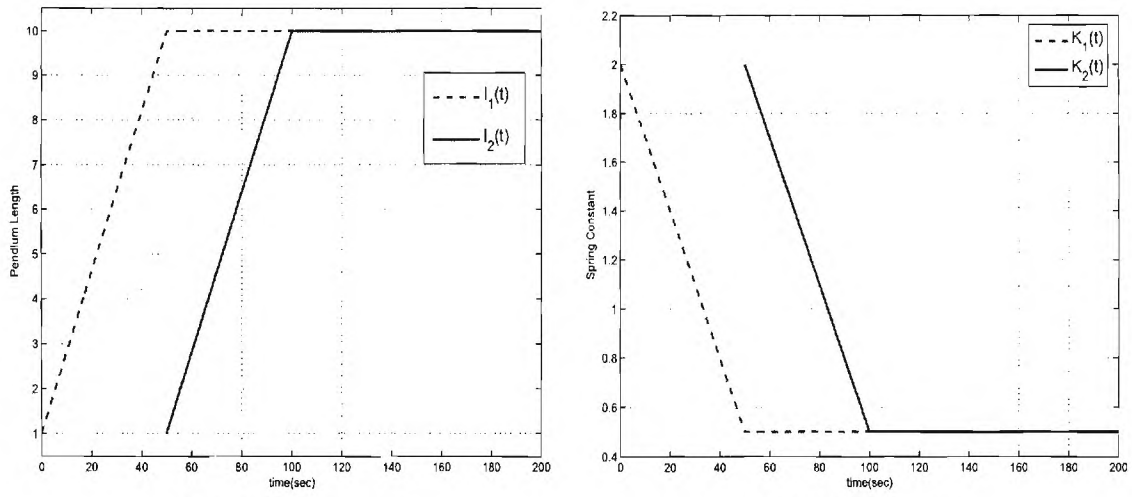

(a) Pendulum length (b) Torsional stiffness

Figure 2.6: Time-varying parameters

where $\widehat{\boldsymbol{W}}(t)$ and $\hat{V}(t)$ are estimate weights for $W(t)$ and $V(t)$ and are adapted on-line. They are update by

$$\begin{aligned}\dot{\widehat{\boldsymbol{W}}} &= -\Gamma_W[(\hat{\boldsymbol{\sigma}} - \hat{\sigma}'\hat{V}^\top\boldsymbol{\eta})\widehat{\boldsymbol{E}}^\top P\bar{\boldsymbol{b}} + k\widehat{\boldsymbol{W}}] \\ \dot{\hat{V}} &= -\Gamma_V[\widehat{\boldsymbol{E}}^\top P\bar{\boldsymbol{b}}\boldsymbol{\mu}\widehat{\boldsymbol{W}}^\top\hat{\sigma}' + k\hat{V}]\,,\end{aligned} \tag{2.41}$$

in which $\Gamma_W, \Gamma_V > 0$ are positive definite adaptation gain matrices, $k > 0$ is a $\sigma-$modification constant, $\hat{\boldsymbol{\sigma}} \triangleq \boldsymbol{\sigma}(\hat{V}\boldsymbol{\eta})$, $\hat{\sigma}'$ is the Jacobian computed at the estimates, P is obtained from (2.36), and $\widehat{\boldsymbol{E}}$ is an estimate for $\boldsymbol{E}$ in (2.34) and is obtained from (2.29), (2.32), and (2.33)

$$\widehat{\boldsymbol{E}} = \begin{bmatrix} e_{i_1} & \hat{e}_{i_2} & x_{dc} \end{bmatrix}^\top, \tag{2.42}$$

instead of designing an observer as done in [29].

In simulation, two SHLNNs whose hidden layer consists of 5 neurons ($N = 5$) are employed for θ_1 and θ_2 dynamics. Since θ_i has the relative degree 2, 2 delayed values of u_i are used, together with 4 delayed values of θ_i to construct an input for each NN[29]. The delay $d = 0.1$, and the parameters for each NN are

$$\Gamma_W = 25I,\ \Gamma_V = 25I,\ k = 1, \tag{2.43}$$

where I is the identity matrix with compatible dimension.

2.3 Simulation Results

Figure 2.6 shows how the structure of the evolving pendulum in Figure 2.2 changes as time evolves. When the first link ($l_1(t)$) finishes its expansion at $t = 50$ sec., the second link ($l_2(t)$) starts to expand and stops its deployment at $t = 100$ sec., where the whole system forms into its final configuration as shown in Figure 2.6(a). Figure 2.6(b) indicates that during deployment, the stiffness of each link declines from 2 to 0.5.

Figure 2.7 shows the time responses of θ_1 and θ_2 when no external disturbances are present. While the open-loop system exhibits large oscillations that are caused by restoring moment of torsional springs,

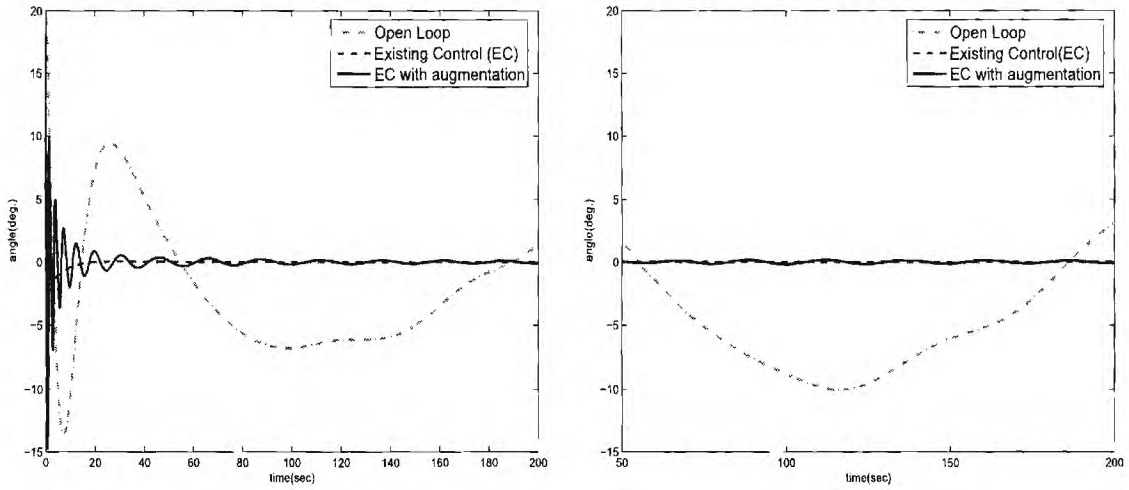

(a) θ_1 (b) θ_2

Figure 2.7: Evolution without any external disturbance

the lead compensator in (2.16) (the Existing Controller) provides good regulation. When the lead compensator is augmented augmented as in Figure 2.5 ("EC with augmentation"), the transient response of θ_1 exhibits fast oscillations caused by initial adaptation of the NN weights. Thus adaptation is not desirable in a benign environment.

Figure 2.8 compares time responses of θ_1 and θ_2 when the structure is subject to the solar pressure torques $f_{s_1}(l_(t), \theta_1)$ and $\boldsymbol{f}_s(l_2(t), \boldsymbol{\theta})$ in (2.4) and (2.9). Since this is the environment in which the sailcraft operates, optimum positioning of the structure before it executes its mission is particularly important. Whereas the existing control system stabilizes the system with much longer settling time as shown in Figure 2.8, with the controller augmented, the time responses for θ_1 and θ_2 are almost the same as those in Figure 2.7 regardless of the solar torque disturbance. Figure 2.9 compares the command tracking performance of the controllers with and without augmentation. While the existing control system fails to regulate the system to the desired position, the augmented system drives the system into a desired set-point.

In general, a spacecraft is less influenced by gravity than are the vehicles on Earth. Nevertheless, atmospheric drag or solar radiation pressure for an orbiting spacecraft can lead to effects that are similar to the effect of gravity, and cause heavy particles to settle toward the front end of a moving spacecraft[30]. In other cases, direct gravitation effects, such as gravity gradient forces due to differences over an extended object, may be required to be taken into account when the spacecraft has a long and slender shape. In our example, when the pendulum evolves along the gravity vector, the gravitational force helps to stabilize the system into its equilibrium position. However, when the structure expands in a direction opposite to that of the gravity vector,the effect of gravity is destabilizing. In the next simulation, we introduce a reduced gravity $g_r = 0.98(m/s^2)$ that is 10% of the gravity on Earth

$$F_{a_x} = \begin{cases} -(m_1 + m_2)g_r & \text{for} \quad 0 < t < t_1 \\ -m_1 g_r & \text{for} \quad t \geq t_1 \end{cases}, \; F_{b_x} = -m_2 g_r \text{ for } \quad t \geq t_1. \tag{2.44}$$

Figure 2.10 shows the time responses of θ_1 and θ_2 with these gravity terms present. Since the zero solution is an unstable equilibrium, the open-loop system goes immediately unstable, and the response for that case is not shown. In this case the lead compensator also fails, and the pendulum falls to a stable

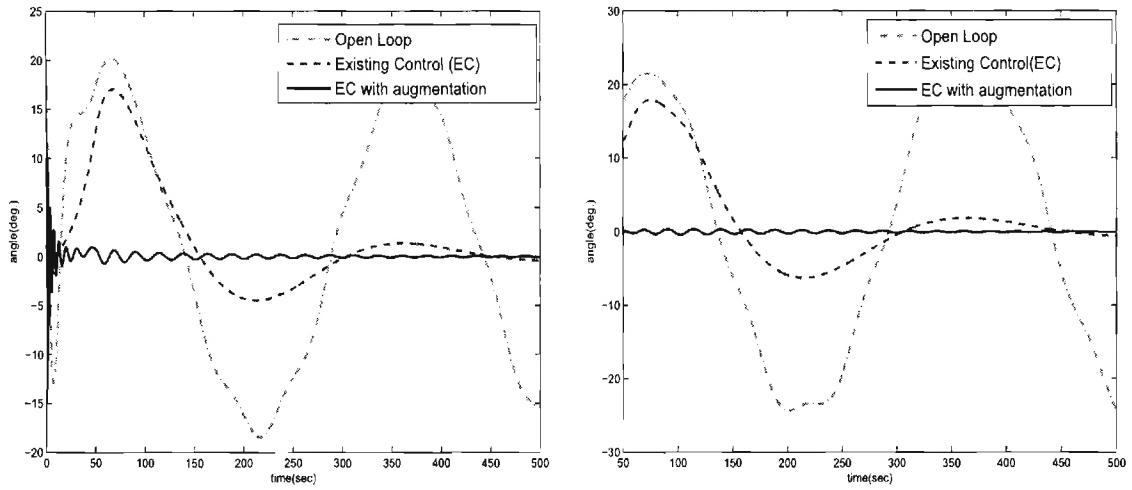

(a) θ_1 (b) θ_2

Figure 2.8: Evolution with the solar pressure

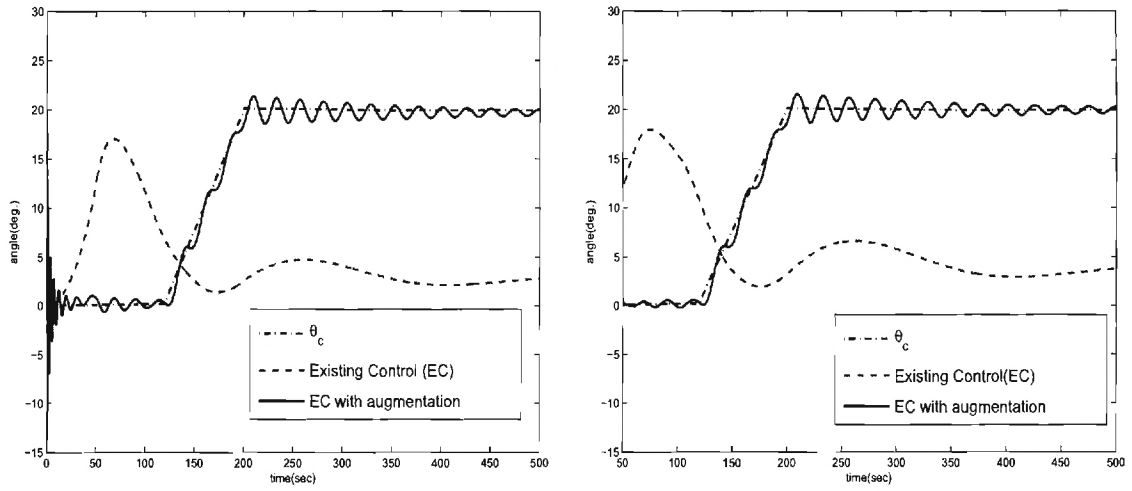

(a) θ_1 (b) θ_2

Figure 2.9: Tracking after evolution with the solar pressure

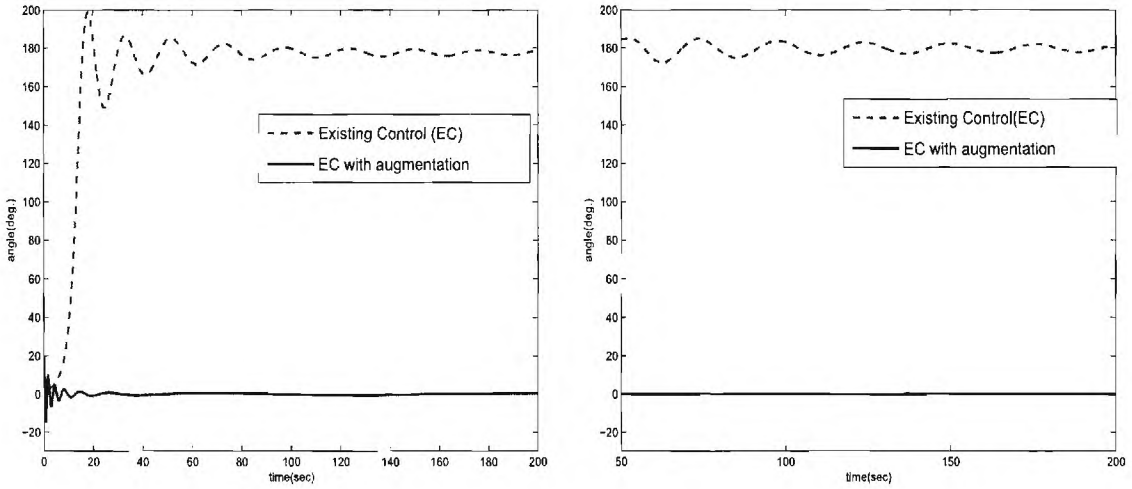

(a) θ_1 (b) θ_2

Figure 2.10: Time responses of the evolving pendulum with the 10% gravitational effect

equilibrium state in which the masses are aligned with the gravity vector. The augmented controller manages to regulate the system to is unstable equilibrium state in which the masses are aligned in opposition to the gravity vector. While the lead compensator in (2.16) fails to restore the pendulum and falls into a stable equilibrium, the augmented controller still regulates the pendulum with respect to its unstable equilibrium. This case is particularly interesting, because every fixed-gain decentralized controller design that was tried failed to regulate the pendulum to its unstable equilibrium condition when subjected to a gravity field. Figure 2.11 compares the time responses with the adaptive signal ("EC+$\nu_{dc} + \nu_{ad}$") to those without the adaptive signal ("EC+ν_{dc}"), and clearly indicates that stable behavior results from adaptive control. This is further confirmed by comparing the modelling errors defined in (2.18), (2.19), and (2.20) to the adaptive signal $\nu_{i_{ad}}$, $i = 1, 2$, in (3.16). Figure 2.12 shows that the adaptive signals closely approximate for the time-varying modelling errors.

2.4 Conclusions

We consider the feasibility of using neural network based adaptive control for evolving gossamer structure which is characterized by time-varying structural properties. A growing double pendulum is used to illustrate the control method. Nominal controllers are designed in a decentralized manner, and augmenting adaptive control elements are added. In a benign environment, the nominal controllers perform well, and successfully stabilize the evolving system. However, when solar radiation pressure or gravitational effects are introduced, the controllers augmented by the adaptive elements significantly outperform the nominal controllers.

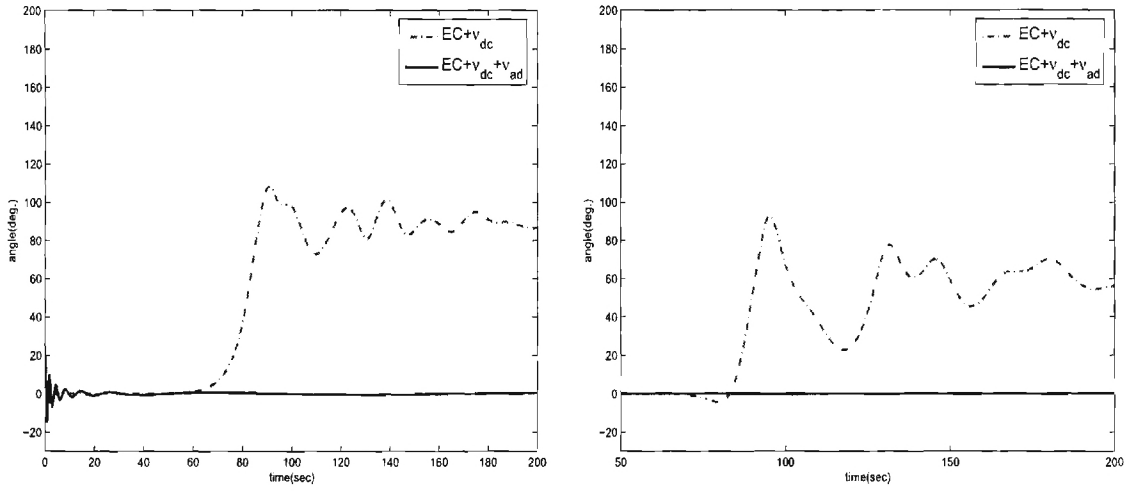

(a) θ_1 (b) θ_2

Figure 2.11: Time responses of the evolving pendulum with and without the adaptive signal ν_{ad} under the 10% gravitational effect

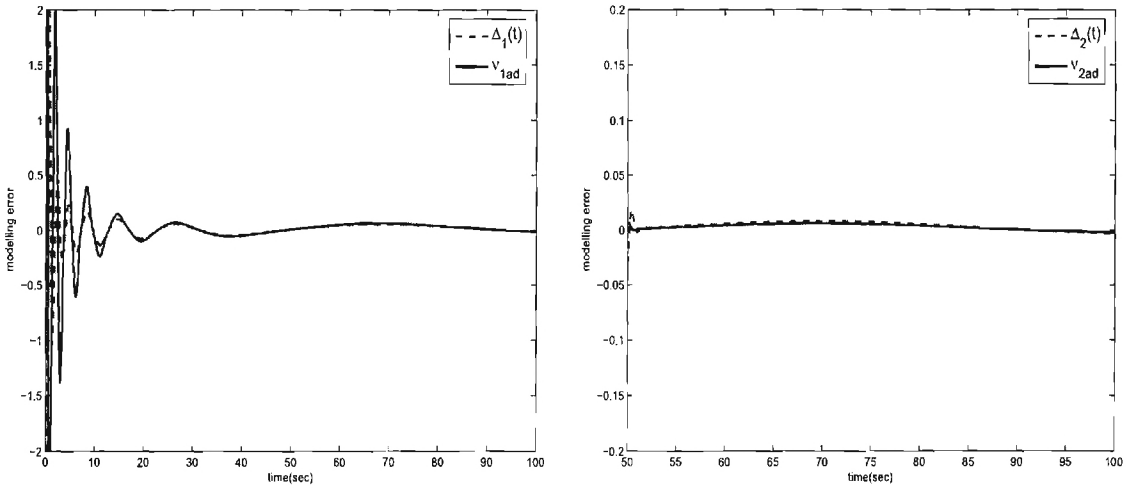

(a) θ_1 (b) θ_2

Figure 2.12: Modelling error and the adaptive signal with the gravitational effect

Section 3

Adaptive Control of Truss Structures for Gossamer Spacecraft

In this section, NN-based adaptive control is considered to address the flexibilities in a truss structure that supports solar sail membranes with the objective being to suppress unwanted vibrations. The SAFE (Solar Array Flight Experiment) boom is used as a test bed for evaluating the adaptive control method. This structure was previously used in a Space Shuttle mission, and it has now been set up for control-structure interaction studies at the NASA Marshall Space Flight Center. In this study, three pairs of collocated accelerometers and air-jet thrusters mounted at the tip of the boom are utilized to suppress unwanted vibrations. The experiment is carried out by considering three-dimensional motions of the boom unlike the previous approaches that only considered planar motions of a truss structure[31, 32, 33, 34]. A critical feature that distinguishes three-dimensional motion from planar motions is the existence of coupling between bending in any two perpendicular directions. Also, as a result of long mission times, the boom may suffer gradual damage that results in inelastic deformation. For example, an inelastic bow in the boom will couple the bending and torsion at the tip where accelerometers and thrusters are mounted. In [35], it is shown that the SAFE boom severely violates Euler-Bernoulli beam model. This poses serious challenges in modelling and control design for the structure. On one hand, structural dynamics are represented using high dimension finite element models. On the other hand, control design requires model-reduction of the finite element model into a manageable state-space model while maintaining its essential features. In this paper, instead of going through this process, we illustrate a NN-based adaptive control design in which a previous linear control design approach, which performed poorly on the current structure, is augmented to account for modeling uncertainty.

In this section, taking the path in [25, 19], a linear controller is designed assuming that bending in the X-Y directions are decoupled from each other as well as from torsion. Two proportional-integral (PI) controllers are designed identically assuming identical modal properties in the X-Y directions. This greatly simplifies the design procedure compared to designing a single controller for the coupled system of dynamics that is not available in our study. Separate but identical NNs are added to compensate for structural uncertainties. Since the PI controllers are intended to control only bending motion in a single direction and the NNs are implemented independently, the overall design is equivalent to the decentralized approach described in [21]. Using experimental tests, we illustrate that the adaptive method is effective in compensating for dead zone nonlinearities present in the thrusters as well as structural uncertainties. The experimental results are further evaluated through comparison with simulation results

in which a PI controller fails to work because of structural uncertainties.

3.1 System Description

3.1.1 Test-bed

Figure 3.1 depicts the SAFE boon, which is 30m long and composed of 132 bays. The experiment is a large flexible structure which has numerous low frequency, coupled,tightly spaced lightly damped modes[36]. Its current hardware includes 12 piezoelectric strain sensors, 12 accelerometers, 9 piezoelectric actuators, and 3 proportional valve air-jet thrusters. In this research, 3 collocated pairs of

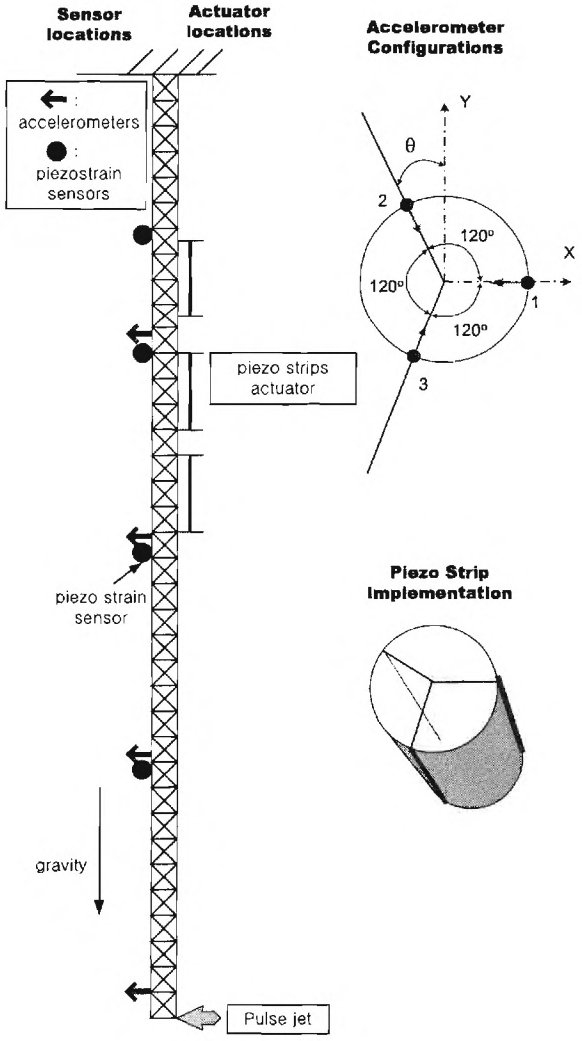

Figure 3.1: SAFE boom test-bed

ADXL320 dual-axis accelerometers from Analog Devices Inc. [37] and EVP proportional control valve air-jet thrusters from Clippard Instrument Laboratory, Inc. [38] are used for vibration suppression tests in a configuration shown on the right upper section in Figure 3.1. The measured acceleration signals are processed by a National Instruments Labview routine before being used in a Labview Real-time software

	X mode		Y mode		Torsion		Z mode	
	ω (Hz)	ζ (%)	ω(Hz)	ζ(%)	ω (Hz)	ζ (%)	ω(Hz)	ζ(%)
1	0.182	1.43	0.185	2.64	2.060	1.7	15.861	0.3
2	0.787	0.93	0.823	0.91	·	·	·	·
3	2.020	5.86	2.141	7.62	·	·	·	·
4	4.061	6.69	4.241	7.03	·	·	·	·

Table 3.1: Modal Coefficients

module which runs at 200 Hz. The controller is imported from Matlab Simulink input-output blocks through the Simulation Interface Toolkit provided by Labview. This make it possible for Simulink blocks that are complied by Simulink Real-time Workshop to be imported as a Labview routine. The control signals from the Labview embedded controller software are converted to 2.5kHz pulse-width modulation (PWM) signal in Labview to drive the EVP valves. As a result, a command from 0 to 1 corresponds to PWM from 0 to 100%. The air begins to flow at approximately 30% PWM signal, and the valve is fully open at 100% PWM signal[38]. Ignoring the PWM block and assuming that the 0-1 signal is proportional to the air jet flow (liters/minute), the actuator can be characterized as shown in Figure 3.2 where $u_i (i = 1, 2, 3)$ is the dimensionless control signal to the Labview PWM routine driving each valve. Note that this actuator presents both a dead zone and a saturation nonlinearity.

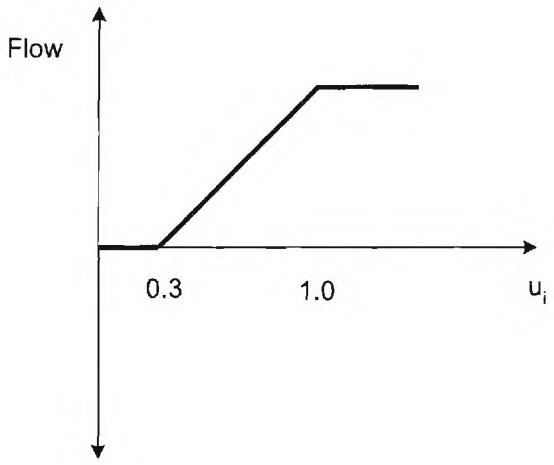

Figure 3.2: Actuator Characteristic

3.1.2 Structural Properties

Table 3.1 shows modal properties obtained by modal analysis of impact data up to 4 bending modes,the first torsional mode, and the first axial mode. In the impact testing, it was observed that X-Y motions are not decoupled, and the modal coefficients in Table 3.1 are mainly used as a guideline for the design of a linear controller for providing damping to the structure. In Section 3.4, these properties are modified to match the experimental data to construct a simulation model.

3.2 Control Design

Figure 3.3 shows the adaptive control architecture in which three thrusters and three accelerometers are treated as the actuators and sensors. Two independent controllers are designed to suppress vibrations

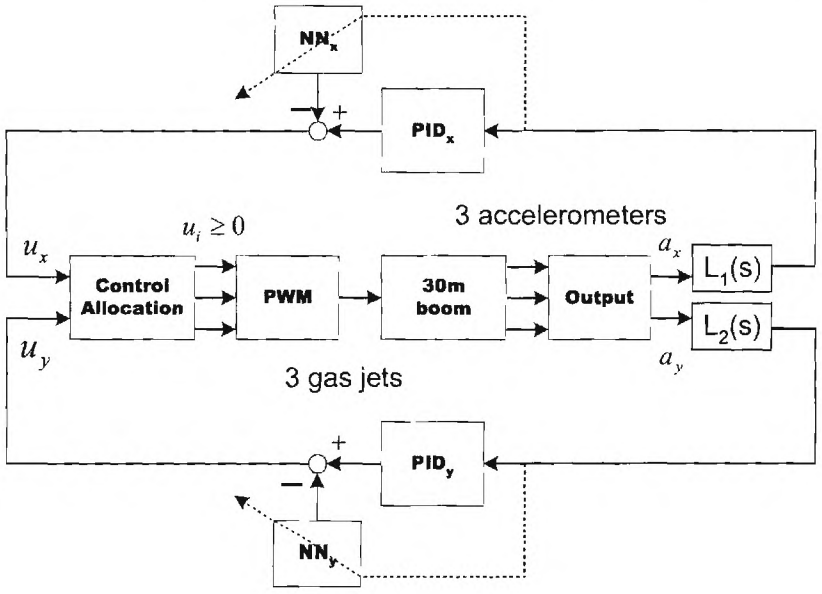

Figure 3.3: Control Architecture

in the X and Y direction, which belongs to the class of decentralized controllers treated in [21].

3.2.1 Output and Control Allocation

Figure 3.4(a) depicts how sensors and actuators are located at the tip of the SAFE boom. Each accelerometer measures accelerations in radial directions and tangential directions. The inertial acceleration $\vec{a} = a_x \boldsymbol{i} + a_y \boldsymbol{j}$ ($\boldsymbol{i}, \boldsymbol{j}$ are unit vectors in X-Y coordinates) at the origin O in Figure 3.4(a) results in the following accelerometer readings in the radial directions:

$$\begin{bmatrix} a_1 \\ a_2 \\ a_3 \end{bmatrix} = \begin{bmatrix} -\cos\phi_1 & -\sin\phi_1 \\ -\cos\phi_2 & -\sin\phi_2 \\ -\cos\phi_3 & -\sin\phi_3 \end{bmatrix} \begin{bmatrix} a_x \\ a_y \end{bmatrix} = \underbrace{\begin{bmatrix} -1 & 0 \\ \sin\theta & -\cos\theta \\ \sin\theta & \cos\theta \end{bmatrix}}_{T} \begin{bmatrix} a_x \\ a_y \end{bmatrix}, \tag{3.1}$$

where $\phi_1 = 0, \phi_2 = 120^o, \phi_3 = 240^o, \theta = 30^o$. Conversely, the accelerations a_x and a_y in Figure 3.3 can be derived from acceleration readings a_i ($i = 1, 2, 3$) as follows:

$$\begin{bmatrix} a_x \\ a_y \end{bmatrix} = (T^\top T)^{-1} T^\top \begin{bmatrix} a_1 \\ a_2 \\ a_3 \end{bmatrix} = \frac{2}{3} \begin{bmatrix} -1 & \sin\theta & \sin\theta \\ 0 & -\cos\theta & \cos\theta \end{bmatrix} \begin{bmatrix} a_1 \\ a_2 \\ a_3 \end{bmatrix}. \tag{3.2}$$

In the same manner, the control signals u_x and u_y in Figure 3.3 should be realized using single directional control signals $u_i \geq 0$ ($i = 1, 2, 3$) that are fed to the PWM routine in Figure 3.3. That is,

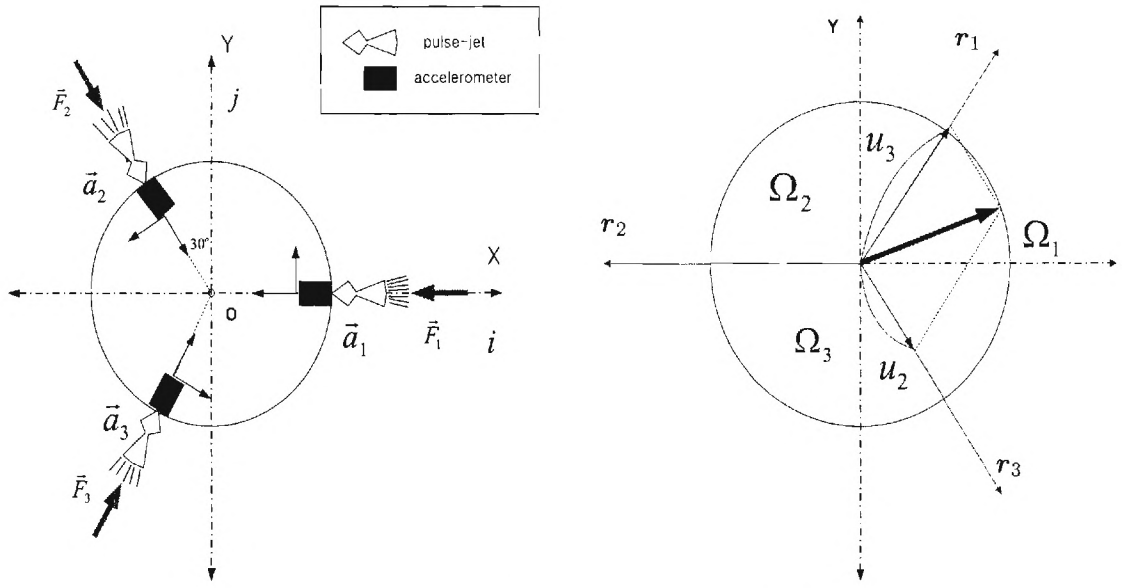

(a) Configuration for accelerometers and air-jet thrusters

(b) Control Allocation

Figure 3.4: Outputs and Control Allocation

the u_i's are determined from $\boldsymbol{u} = u_x\boldsymbol{i} + u_y\boldsymbol{j} = u_1\boldsymbol{r}_1 + u_2\boldsymbol{r}_2 + u_3\boldsymbol{r}_3$, where $\boldsymbol{r}_i$ is a unit vector aligned with the thrust axis of the ith thruster. This leads to

$$\begin{bmatrix} u_x \\ u_y \end{bmatrix} = \begin{bmatrix} -1 & \sin\theta & \sin\theta \\ 0 & -\cos\theta & \cos\theta \end{bmatrix} \begin{bmatrix} u_1 \\ u_2 \\ u_3 \end{bmatrix} = T^\top \begin{bmatrix} u_1 \\ u_2 \\ u_3 \end{bmatrix}. \tag{3.3}$$

Nonnegative solutions for each u_i are determined as follows. After a region to which $\boldsymbol{u}$ belongs is determined, $\boldsymbol{u}$ is realized using two nonnegative components. For example, Figure 3.4(b) illustrates how $\boldsymbol{u} \in \Omega_1$ can be realized by u_2 and u_3. A region to which $\boldsymbol{u}$ belongs is decided using a parameter $R = \mathsf{atan2}(u_y, u_x)$. As a result, control signals u_i are allocated as follows.

1. $\boldsymbol{u} \in \Omega_1$ $(-\frac{\pi}{3} \le R \le \frac{\pi}{3})$
   $u_1 = 0$, and u_2, u_3 are determined by $\begin{bmatrix} u_x \\ u_y \end{bmatrix} = \begin{bmatrix} \sin\theta & \sin\theta \\ -\cos\theta & \cos\theta \end{bmatrix} \begin{bmatrix} u_2 \\ u_3 \end{bmatrix}$.
2. $\boldsymbol{u} \in \Omega_2$ $(\frac{\pi}{3} < R \le \pi)$
   $u_2 = 0$, and u_1, u_3 are determined by $\begin{bmatrix} u_x \\ u_y \end{bmatrix} = \begin{bmatrix} -1 & \sin\theta \\ 0 & \cos\theta \end{bmatrix} \begin{bmatrix} u_1 \\ u_3 \end{bmatrix}$.
3. $\boldsymbol{u} \in \Omega_3$ $(-\pi \le R < -\frac{\pi}{3})$
   $u_3 = 0$, and u_1, u_2 are determined by $\begin{bmatrix} u_x \\ u_y \end{bmatrix} = \begin{bmatrix} -1 & \sin\theta \\ 0 & -\cos\theta \end{bmatrix} \begin{bmatrix} u_1 \\ u_2 \end{bmatrix}$.

3.2.2 Linear Controllers

Since we are interested in frequencies below 3 Hz, the acceleration signals are filtered by low-pass filters $L_i(s)$ $(i = 1, 2)$ as shown in Figure 3.3, where

$$L_i(s) = \frac{1}{s/\omega_l + 1}, \ \omega_l = 6(Hz) = 12\pi(rad/sec), \ i = 1, 2. \tag{3.4}$$

PI controllers are designed under the assumption that X-Y dynamics are decoupled. Since Table 3.1 only provides modal properties of the structure, developing a high-fidelity structural model that includes actuator nonlinearities is a time-consuming procedure. Instead of attempting an elaborate model based control design, all the nonlinearities are neglected, and the following simplified structural model is used for control design

$$\begin{aligned} &\ddot{q}_{x_i} + 2\zeta_{x_i}\omega_{x_i}\dot{q}_{x_i} + \omega_{x_i}^2 q_{x_i} + \phi_{x_i}(\boldsymbol{s}) = b_{x_i}u_x \\ &\ddot{q}_{y_i} + 2\zeta_{y_i}\omega_{y_i}\dot{q}_{y_i} + \omega_{y_i}^2 q_{y_i} + \phi_{y_i}(\boldsymbol{s}) = b_{y_i}u_y, \quad i = 1, 2, \\ &a_x = K_s\ddot{x}, \\ &a_y = K_s\ddot{y}, \end{aligned} \tag{3.5}$$

where q_{x_i} and q_{y_i} represent modal displacements, the displacement in the X-Y directions are given by $x = q_{x_1} + q_{x_2}$, $y = q_{y_1} + q_{y_2}$, and $\boldsymbol{s} = [x, y, \dot{x}, \dot{y}]^\top$. The variables a_x and a_y are accelerations in the X and Y directions, and the corresponding modal coefficients are given in Table 3.1. The parameter values: $b_{x_1} = 0.9$, $b_{x_2} = 0.1$, $b_{y_1} = 0.7$, $b_{y_2} = 0.3$, $K_s = 0.034$ were selected to match the experimental data from open-loop response tests. The terms $\phi_{x_i}(\boldsymbol{s})$ and $\phi_{y_i}(\boldsymbol{s})$ are lumped uncertainties that represent the effect of modeling error. If $\phi_{x_i}(\boldsymbol{s}) = \phi_{y_i}(\boldsymbol{s}) = 0$, the transfer function for the X-direction is given by

$$\frac{a_x(s)}{u_x(s)} := G_x(s) = K_x \frac{s^2(s^2 + 2\zeta_z\omega_z s + \omega_z^2)}{(s^2 + 2\zeta_1\omega_1 s + \omega_1^2)(s^2 + 2\zeta_2\omega_2 s + \omega_2^2)}, \tag{3.6}$$

where $K_x = 0.034, \omega_z = 4.66 \ rad/s(= 0.7417Hz), \zeta_z = 0.009, \omega_1 = 1.1435 \ rad/s(= 0.182Hz), \omega_2 = 4.9449 \ rad/s(= 0.787Hz), \zeta_1 = 0.0143, \zeta_2 = 0.0093$. A PI controller is designed based on the transfer function in (3.6) using MATLAB SISO tool. Figure 3.5 shows the root locus plot and loop gain bode plot when the PI controller is given by

$$G_c(s) = K_p \frac{s + z_c}{s}, \tag{3.7}$$

where $K_p = 2$, $z_c = -0.5$. The closed loop poles are located at $-40.2, 0, -0.050 \pm 4.89j, -0.0306 \pm 1.1j$. The damping ratio has increased from 0.0143 to 0.0279 while the natural frequency has slightly decreased from 1.1435 rad/s to 1.10 rad/s for the first mode. The second mode has a damping ratio of 0.010 and natural frequency of 4.89 rad/s. Therefore, the PI controller mainly adds damping to the first mode and has little influence on the second mode. The same controller is used in the Y direction.

3.2.3 Adaptive Control

Two SHLNNs are used to compensate for uncertainties in the system dynamics as shown in Figure 3.3. The design approach follows the method in [20] in which an adaptive design approach for a relative degree one nonminimum phase system is presented with acceleration as a regulated variable. Since adaptive controllers are augmented identically for both X and Y directions, subscript x and y are dropped for simplicity of presentation in what follows.

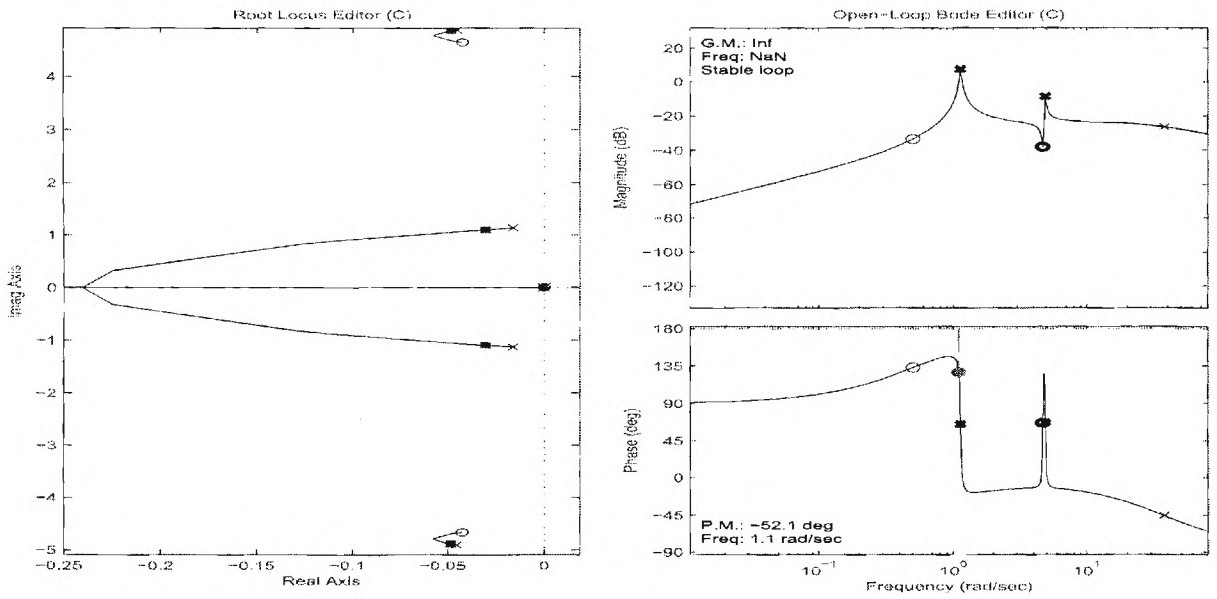

Figure 3.5: root locus and loop gain plots when the transfer function in (3.6) is regulated by the PI controller in (3.7)

Since the acceleration in (3.6) has relative degree zero with respect to the control input u_x, a filtered acceleration is chosen as the regulated output,

$$a_f = L_1(s)a_x, \tag{3.8}$$

which has relative degree one. From this point, the method is identical to that in [20]. With a_f as the regulated output, the systems in (3.5) and (3.8) can be put in a normal form whose first line becomes

$$\dot{a}_f = -w_l a_f - w_l K_s \sum_{i=1}^{2} (2\zeta_i \omega_i \dot{q}_i + \omega_i^2 q_i) + w_l K_s (u + \Delta(\boldsymbol{s})), \tag{3.9}$$

where the matched uncertainty $\Delta(\boldsymbol{s})$ is given by

$$\Delta(\boldsymbol{s}) = -\sum_{i=1}^{2} \phi_i(\boldsymbol{s})). \tag{3.10}$$

Let

$$u = u_{lc} - u_{ad}, \tag{3.11}$$

where u_{lc} is the PI control signal, and u_{ad} is the adaptive signal to compensate for the uncertainty. Since the acceleration is regulated to zero, the reference model in [20] is simply zero, and the tracking error is given by

$$e = 0 - a_f = -a_f. \tag{3.12}$$

A SHLNN is used to approximate the matched uncertainty $\Delta(\boldsymbol{s})$ in (3.10) using a memory unit of sampled input/output pairs. Following the NN approximation property in [16], the matched uncertainty is parameterized

$$\Delta(\boldsymbol{\eta}) = \boldsymbol{W}^\top \boldsymbol{\sigma}(V^\top \boldsymbol{\eta}) + \varepsilon(\boldsymbol{\eta}), \ |\varepsilon(\boldsymbol{\eta})| \leq \epsilon^*, \tag{3.13}$$

on a compact domain of interest under the assumption that the system dynamics are observable with respect to the regulated output. The term $\varepsilon(\boldsymbol{\eta})$ is the NN reconstruction error, which is upper bounded by ϵ^* on the approximation domain, and $\boldsymbol{\eta}$ is the network input vector

$$\begin{aligned}\boldsymbol{\eta}(t) &= [\ 1 \quad \bar{\boldsymbol{u}}_d^\top(t) \quad \bar{\boldsymbol{y}}_d^\top(t)\ ]^\top, \\ \bar{\boldsymbol{u}}_d^\top(t) &= [u(t) \quad u(t-d) \quad \cdots u(t-(n_1-r-1)d)]^\top, \\ \bar{\boldsymbol{y}}_d^\top(t) &= [a_f(t) \quad a_f(t-d)\cdots a_f(t-(n_1-1)d)]^\top,\end{aligned} \tag{3.14}$$

in which n_1 is the length of the window and is generally required to be greater than or equal to the system dimension, $d > 0$ is a time-delay, r is the relative degree of the output (one for a_f), $\boldsymbol{\sigma}$ is a vector of squashing functions, $\sigma(\cdot)$, whose i^{th} element is defined as $\left[\boldsymbol{\sigma}(V^\top\boldsymbol{\eta})\right]_i = \sigma\left[(V^\top\boldsymbol{\eta})_i\right]$. The squashing functions are chosen as sigmoidal functions

$$[\boldsymbol{\sigma}(V^\top\boldsymbol{\eta})]_i = \frac{1}{1+e^{-a(V^\top\boldsymbol{\eta})}},\ i = 1,\ldots,N, \tag{3.15}$$

where $a = 1$ represents the activation potential, and N is the number of neurons in the hidden layer.

The adaptive signal u_{ad} is designed as

$$u_{ad} = \widehat{\boldsymbol{W}}(t)^\top\boldsymbol{\sigma}(\widehat{V}(t)^\top\boldsymbol{\eta}) \tag{3.16}$$

where $\widehat{\boldsymbol{W}}(t)$ and $\widehat{V}(t)$ are estimates for the ideal weights that are adapted on-line. The update law for $\widehat{\boldsymbol{W}}(t)$ and $\widehat{V}(t)$ follows from that in [20]

$$\begin{aligned}\dot{\widehat{\boldsymbol{W}}} &= -\Gamma_W[(\hat{\boldsymbol{\sigma}} - \hat{\sigma}'\widehat{V}^\top\boldsymbol{\eta})e + k_\sigma\widehat{\boldsymbol{W}}] \\ \dot{\widehat{V}} &= -\Gamma_V[e\boldsymbol{\eta}\widehat{\boldsymbol{W}}^\top\hat{\sigma}' + k_\sigma\widehat{V}],\end{aligned} \tag{3.17}$$

in which $\Gamma_W, \Gamma_V > 0$ are positive definite adaptation gain matrices, $k_\sigma > 0$ is a $\sigma-$modification constant, $\hat{\boldsymbol{\sigma}} \triangleq \boldsymbol{\sigma}(\hat{V}\boldsymbol{\eta})$, $\hat{\sigma}'$ is the Jacobian computed at the estimates.

In implementation, the SHLNN consists of 5 neurons ($N = 5$), and 8 delayed values of the output, together with 7 delayed inputs, are used to construct the NN input $\boldsymbol{\eta}$ ($n_1 = 8$ and $r = 1$). The time delay $d = 0.01$ sec., and the parameters for the NN are

$$\Gamma_W = 1I,\ \Gamma_V = 1I,\ k_\sigma = 1, \tag{3.18}$$

where I is the identity matrix with compatible dimension.

3.3 Experimental Results

The experiment was performed by applying three cycles of a 0.17Hz sinusoidal disturbance voltage to the thruster located at the tip in the X-direction. After the disturbance, the control thrusters are activated at 20 sec. When the PI controller in (3.7) is implemented, the closed-loop system immediately went unstable with further tweaking gains for K_p and K_i not being able to recover stability. Selecting $K_i = 0$ and $K_p = 1$ results in the stable system, whose acceleration responses are shown in Figure 3.6. Notice that the disturbance in the X-direction leads to an acceleration in Y-direction due to structural coupling as shown in Figure 3.6(b). Moreover, the proportional (P) controller results in almost identical responses to those of the open-loop system, implying that the proportional controller is not effective in suppressing vibrations. Figure 3.7(a) reveals that the control voltages applied to PWM never exceeded

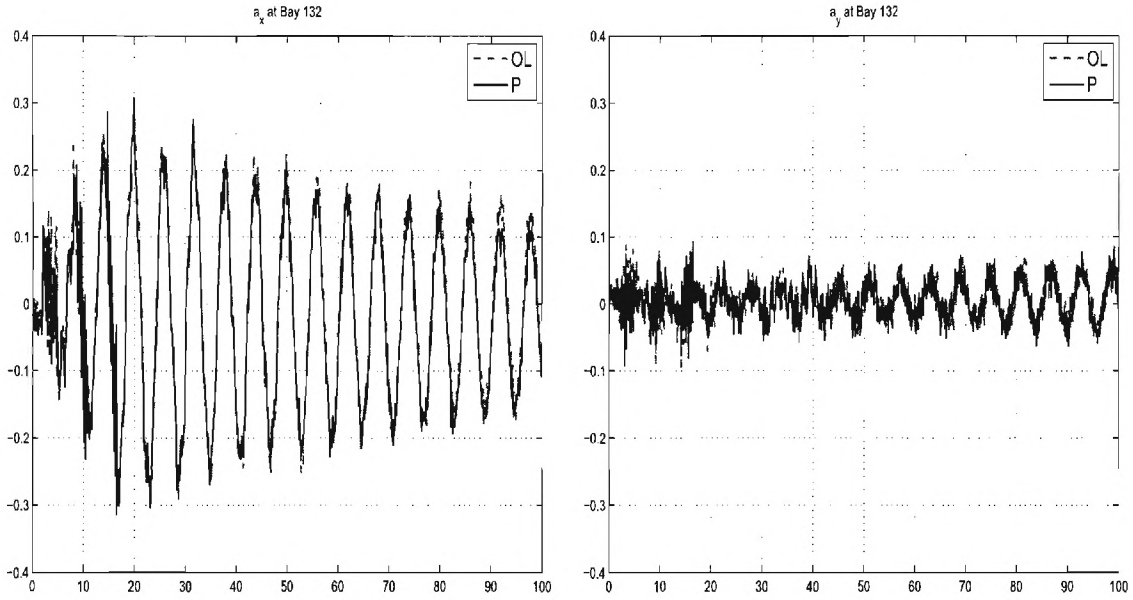

(a) a_x (b) a_y

Figure 3.6: Acceleration responses to the initial disturbances

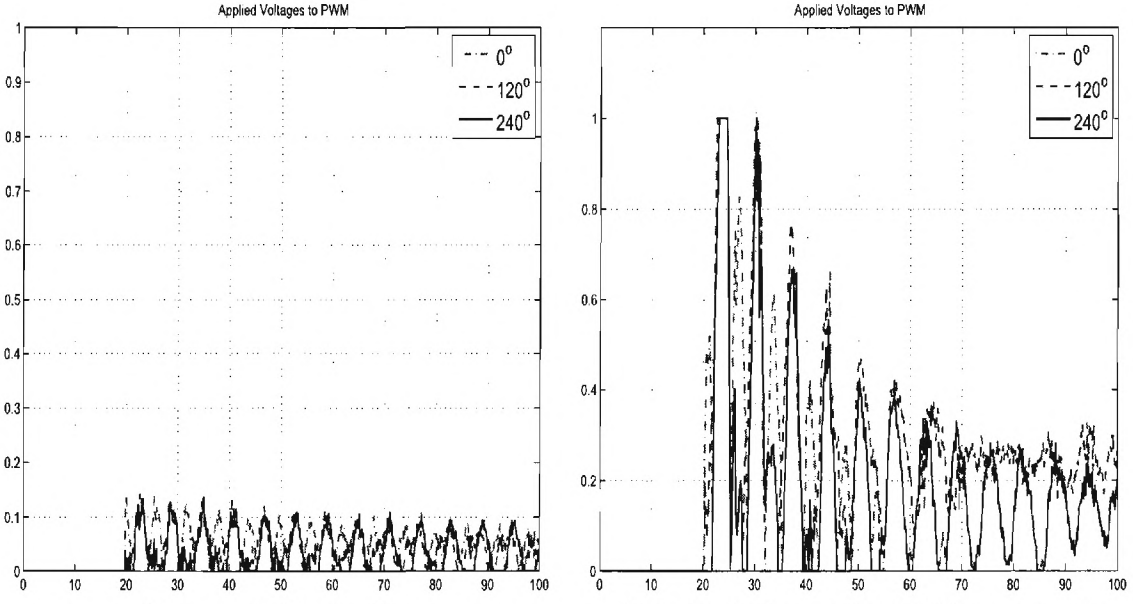

(a) u_i for the P controller (b) u_i for the P controller with NN augmented

Figure 3.7: Applied Control Voltages to PWM

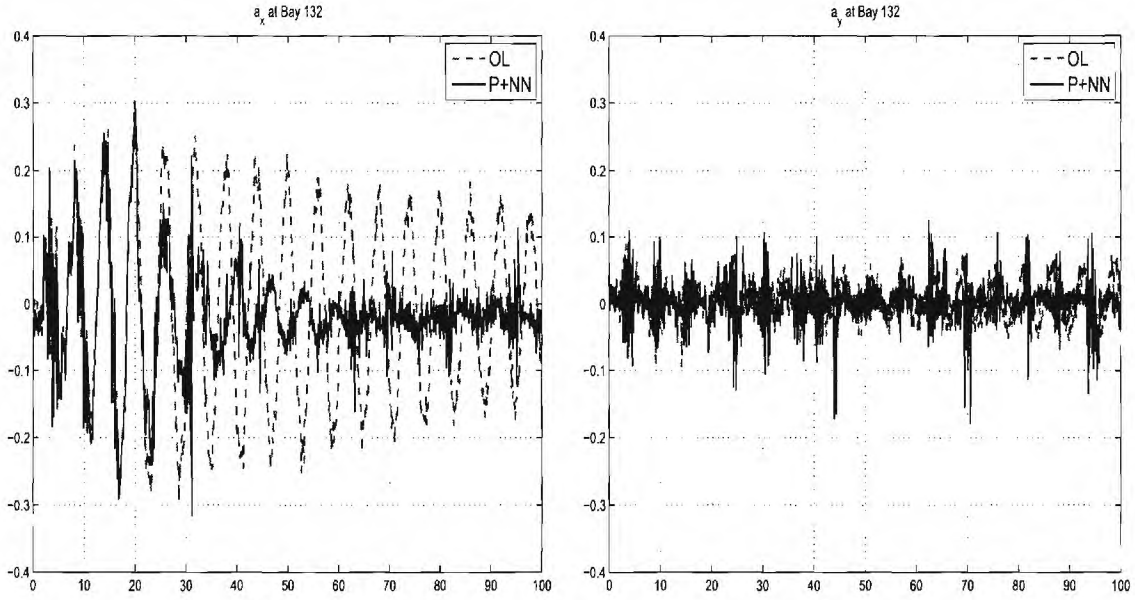

(a) a_x (b) a_y

Figure 3.8: Comparison of acceleration responses of the open-loop to those with the P controller augmented by the NN

the dead zone value, and the P controller essentially resulted in open-loop responses.

Whereas a stabilizing combination for K_p and K_i was not found, generally proportional velocity feedback should be able to provide damping[39]. However, since a velocity sensor is not available, this can only be approximated by pure integral feedback. When a pure integral controller ($K_p = 0$ and $K_i = 0.2$) was implemented, the accelerometer bias caused the integrator to wind up and the structure was displaced to a point in which the thrusters with fully open valves are in balance with the recovering force due to structural stiffness.

Figure 3.8 shows the acceleration responses when the P controller is augmented by the NN ("P+NN"). The vibrations in X-direction are well suppressed by the thrusters, and the accelerations in the X-Y directions subsides to the same level. Figure 3.7(b) shows that with the NN augmented, the dead zone nonlinearity is overcome by the adaptive signal. Comparing Figure 3.7(b) to Figure 3.8(b) reveals that spikes in a_y occur when a pair of thrusters are switched into a different pair according to the control allocation method in Section 3.2-3.2.1. This implies that non-perfect synchronization in the thrusters caused the spikes. Acceleration responses and control voltages are shown in Figures 3.9 and 3.10 for the case where a continuous sinusoidal disturbance is applied in the X direction. Figure 3.10(a) reveals that with the P controller the control signal does not exceed the actuator dead zone and the responses in Figure 3.9(a) are essentially the same as the open-loop responses which exhibit resonant behavior. With the P controller augmented by the NN, Figure 3.9(b) shows that the external disturbances are well attenuated.

3.4 Uncertainty Modeling

In this section, we further investigate, 1) the possibility of using a washed out integrator (an integrator with its pole shifted slightly into the left hand plane), 2) the significance of actuator dead zone, and 3)

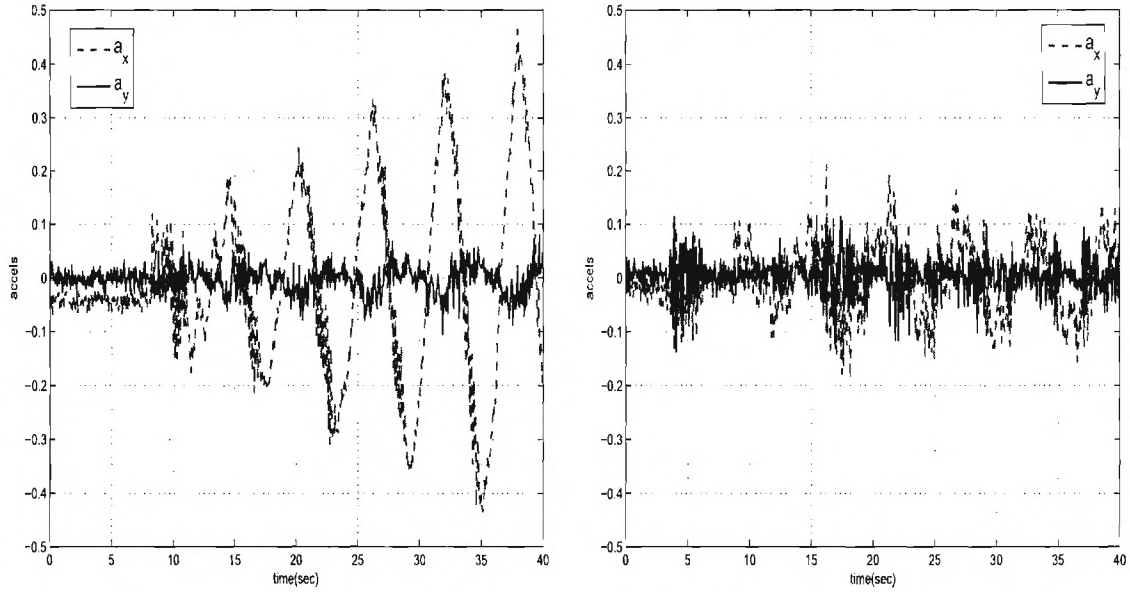

(a) a_x and a_y without NN

(b) a_x and a_y with the NN

Figure 3.9: Acceleration responses to continual external disturbances

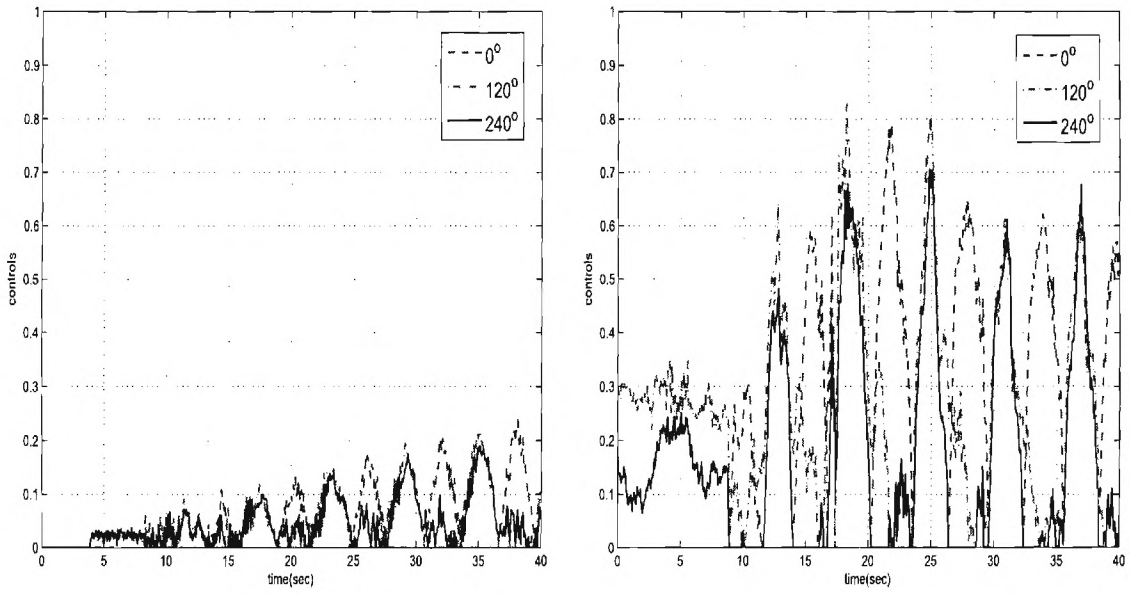

(a) u_i without the NN

(b) u_i with the NN

Figure 3.10: Control signals with continuous external disturbances

the effect of structural uncertainty.

3.4.1 Simulation Model

In Section 3.2-3.2.2, the linear model based on modal coefficients in Table 3.1 was used to design the PI controller in (3.7) ($\phi_{x_i} = \phi_{y_i} = 0$). In this section specific choices for the terms ϕ_{x_i}, ϕ_{y_i} are introduced to approximate the X-Y coupling accelerations observed experimentally:

$$\begin{aligned} \phi_{x_1}(x,y) &= -\alpha_{x_1}x^3 - \beta_{y_1}(y^2 + 0.1y^3), \phi_{x_2}(x,y) = -\alpha_{x_2}x^3 - \beta_{y_2}(y^2 + 0.1y^3) \\ \phi_{y_1}(x,y) &= -\alpha_{y_1}y^3 - \beta_{y_1}(x^2 + 0.1x^3), \phi_{y_2}(x,y) = -\alpha_{y_2}y^3 - \beta_{y_2}(x^2 + 0.1x^3), \end{aligned} \tag{3.19}$$

where $\alpha_{x_1} = 0.3$, $\alpha_{x_2} = 0.1$, $\alpha_{y_1} = 0.2$, $\alpha_{y_2} = 0.1$, $\beta_{x_1} = \beta_{x_2} = \beta_{y_1} = \beta_{y_2} = 0.5$. These terms are derived considering a coupled mass-spring motion in the X and Y directions, and they do no affect the linearized dynamics. Actuation nonlinearity is also introduced in (3.5) using

$$\begin{bmatrix} u_x \\ u_y \end{bmatrix} = T^\top \begin{bmatrix} g(u_1) \\ g(u_2) \\ g(u_3) \end{bmatrix}, \tag{3.20}$$

where the function g is depicted in Figure 3.2. With the nonlinearities in (3.19) and (3.20), when the system in (3.5) is subjected to the same disturbance used to obtain the results in Figure 3.6, the simulated response produced a smaller settling time. Therefore, to match the experimental data, the damping coefficient for the first mode in X-direction was reduced to 0.3%. Figure 3.11 compares the resulting simulation responses to the experimental data. While Figure 3.11(a) shows that the frequency and the damping for the first mode matches those of the experimental data, the acceleration a_y in Figure 3.11(b) does not agree that well. This is due to the fact that the accelerations in the Y-direction stem from the unknown structural coupling, and the coupling nonlinearities in (3.5) are artificially devised. Nevertheless, it was felt that the match between the experimental and simulated accelerations in the Y axis are adequate for a qualitative analysis.

3.4.2 A PI controller with a washed out integrator

A PI controller with a washed out integrator is approximated using

$$G_c(s) = K_p + K_i \frac{1}{s + 1/\tau_h}, \tag{3.21}$$

where $K_p = 0.5, K_i = 0.2$, and $\tau_h = 3.2$. Figure 3.12 shows the root locus plot (K_p is varied with a zero fixed at $-(\frac{1}{\tau_h} + \frac{K_i}{K_p}) = -0.7$) and the loop gain frequency response with the controller in (3.21). When the controller in (3.21) was implemented in the experiment, the integrator still wound up quickly while this was not observed in simulation. This means that the instability is not caused by accelerometer bias. In Figure 3.13, the simulated acceleration responses of the nominal closed-loop system in which $\phi_{x_i} = \phi_{y_i} = 0$ ("the plant model without coupling terms") are compared to those of the open-loop model in (3.5) in which ϕ_{x_i}, ϕ_{y_i} are given by (3.19) ("OL"). More simulated accelerations are shown in Figure 3.14 for the cases where the PI controller is applied with and without the dead zone ("the plant model with dead zone" and "the plant model without dead zone"). While the PI controller reduces acceleration responses without nonlinearity, comparing Figure 3.13 and 3.14 (see "OL" and " the plant model with dead zone") shows that the PI controller does not overcome the dead zone and results in an acceleration response identical to that of the open-loop system. Moreover, Figure 3.14 shows that the

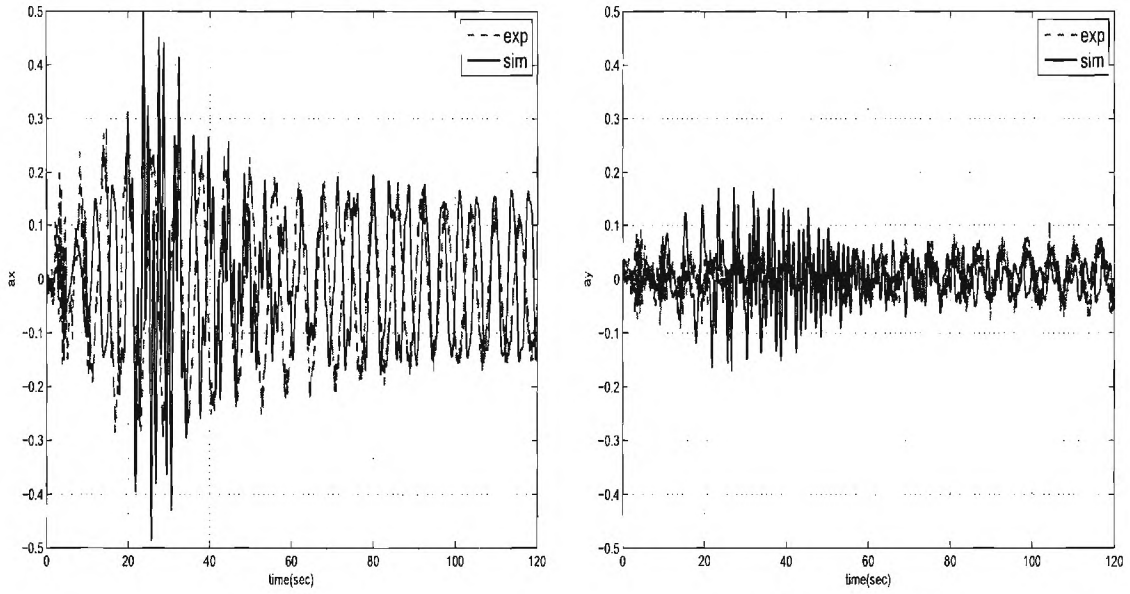

(a) a_x (b) u_i with the NN

Figure 3.11: Comparison of Simulation model and the experimental data

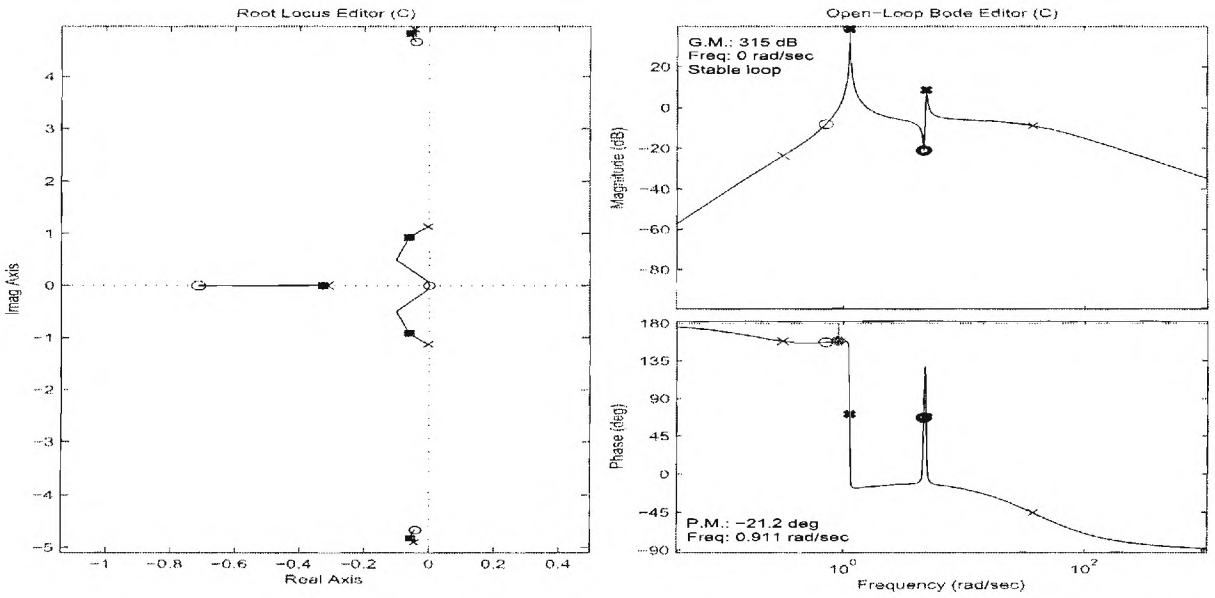

Figure 3.12: root locus and loop gain plots when the transfer function in (3.6), with $\zeta_1 = 0.003$, is regulated by the controller in (3.21)

controller is not effective in the absence of the dead zone in the actuator. That is, the controller applied to the model with the coupling terms ϕ_{x_i} and ϕ_{y_i} fails to effectively suppress vibrations whether the dead zone is present or not. This illustrates that the PI controller is not effective when the nonlinearities of displacements are present, implying that the presence of nonlinear coupling terms makes it extremely difficult to find a working PI controller.

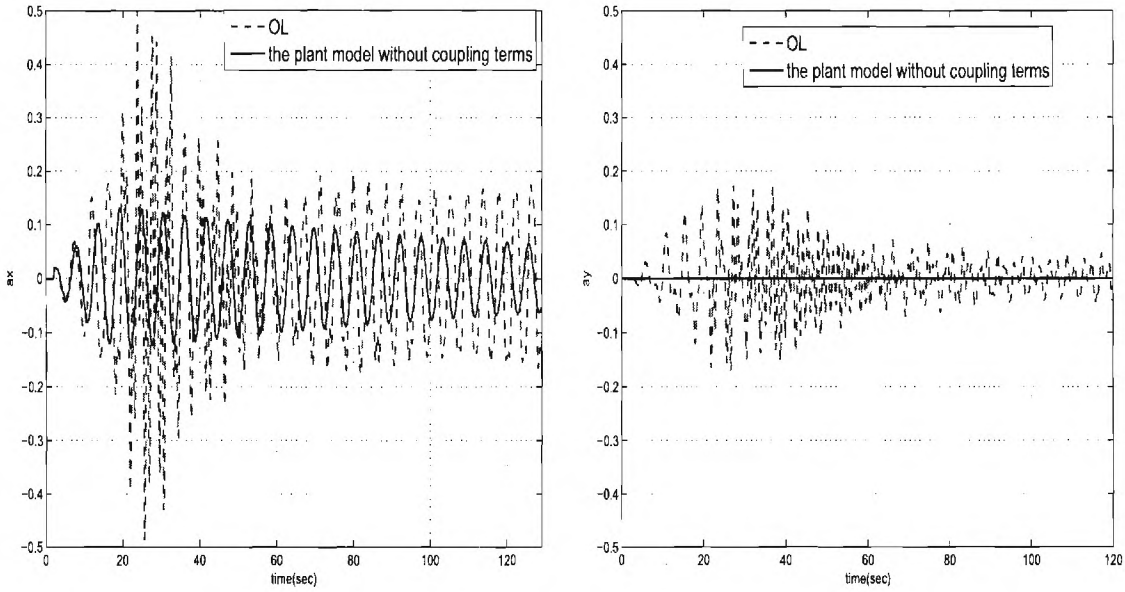

(a) a_x (b) a_y

Figure 3.13: Comparison of the open-loop responses to the plant model regulated by the controller in (3.21) in the absence of nonlinear terms

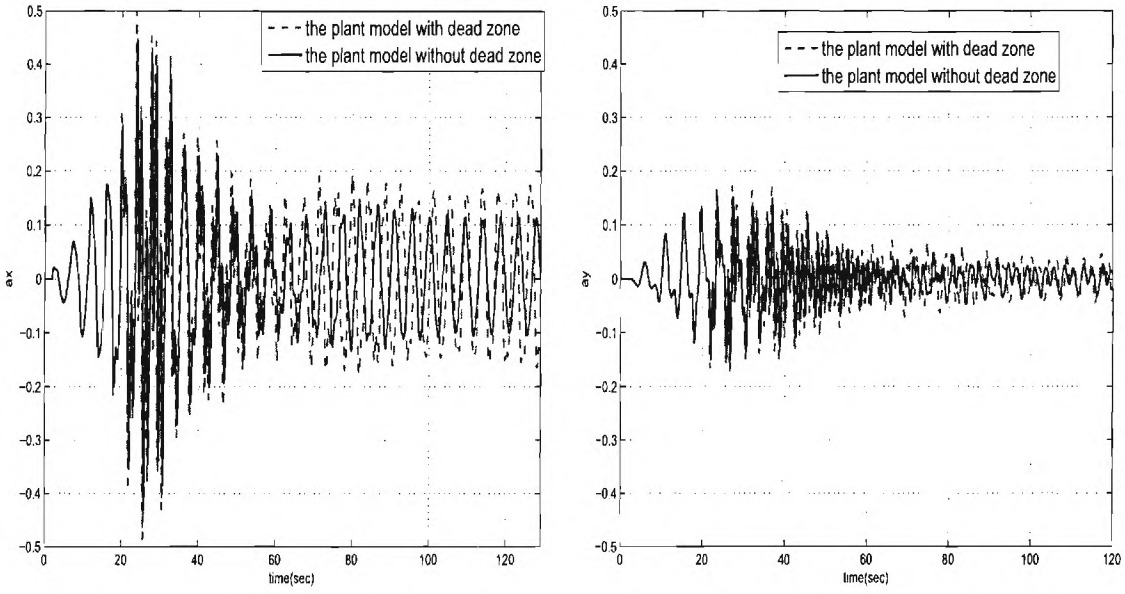

(a) a_x (b) a_y

Figure 3.14: Comparison of the closed-loop system regulated by the controller in (3.21) with and without the dead zone

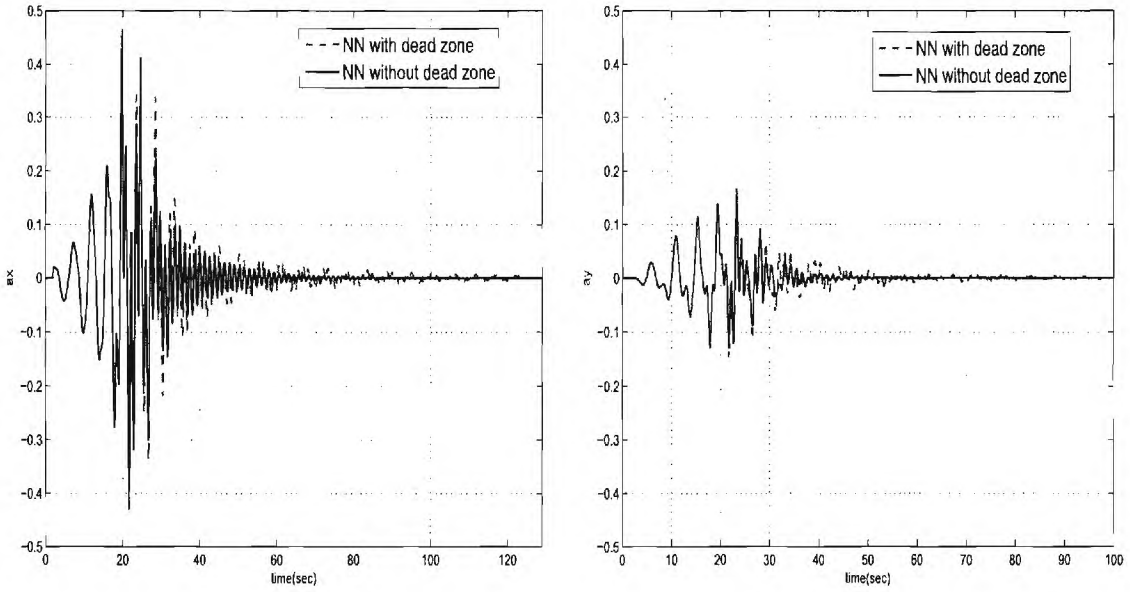

(a) a_x (b) a_y

Figure 3.15: Acceleration responses when the controller in (3.21) is augmented by a NN with and without dead zone

3.4.3 The role of adaptation

Figure 3.15 shows acceleration responses when the controller in (3.21) is augmented by a NN with and without the dead zone nonlinearity. The control signal is activated at 20 sec. as in experimental results in Figure 3.8. The adaptive signals compensate for both structural nonlinearities and the effect of dead zone. This is evidenced by the fact that there is little difference between the responses with and without the dead zone. Moreover, since the control architecture in Figure 3.3 does not involve a reference model, the NN augmented controllers produce nearly the same acceleration responses when augmenting the P and the PI controllers. This is shown in Figure 3.16. This is not surprising because the linear controllers, whether they are the P controller or the PI controllers, do not overcome the dead zone nonlinearities, and the control signals are dominated by the adaptive signals.

Finally, simulation results in which the model in (3.21) is regulated by the P controllers with NNs augmented are compared to the experimental data in which the structure is regulated by the same controller in Figure 3.17. Considering that the nonlinearities in the simulation model are either idealized or arbitrarily introduced, it is interesting that two results are in good agreement except those spikes caused by non-perfect synchronization in the thrusters. In essence, Figure 3.17 indicates that the NNs were effective in compensating for uncertainties that arise due to nonlinear actuation, couplings effects between the X-Y dynamics, and unmodeled dynamics both in simulations and in the real implementation.

3.5 Conclusions

We consider the feasibility of using neural network based adaptive control for a truss structure that may be used to support a solar sail membrane. An experimental study was performed using the SAFE

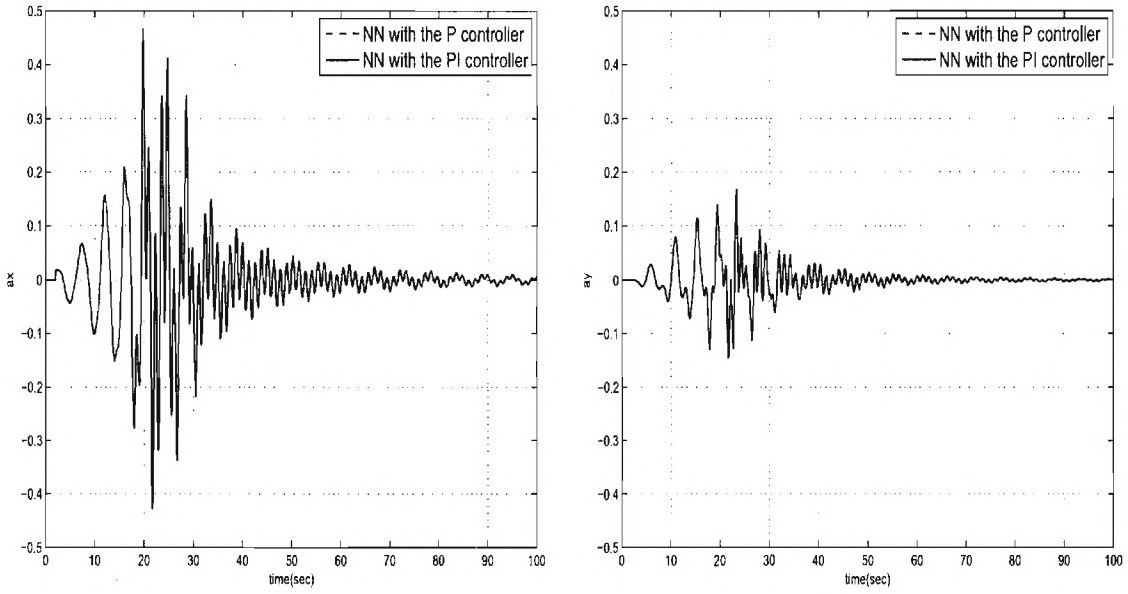

(a) a_x (b) a_y

Figure 3.16: Acceleration responses when the controller in (3.21) and the P controller in Section 3.3 are augmented by NNs

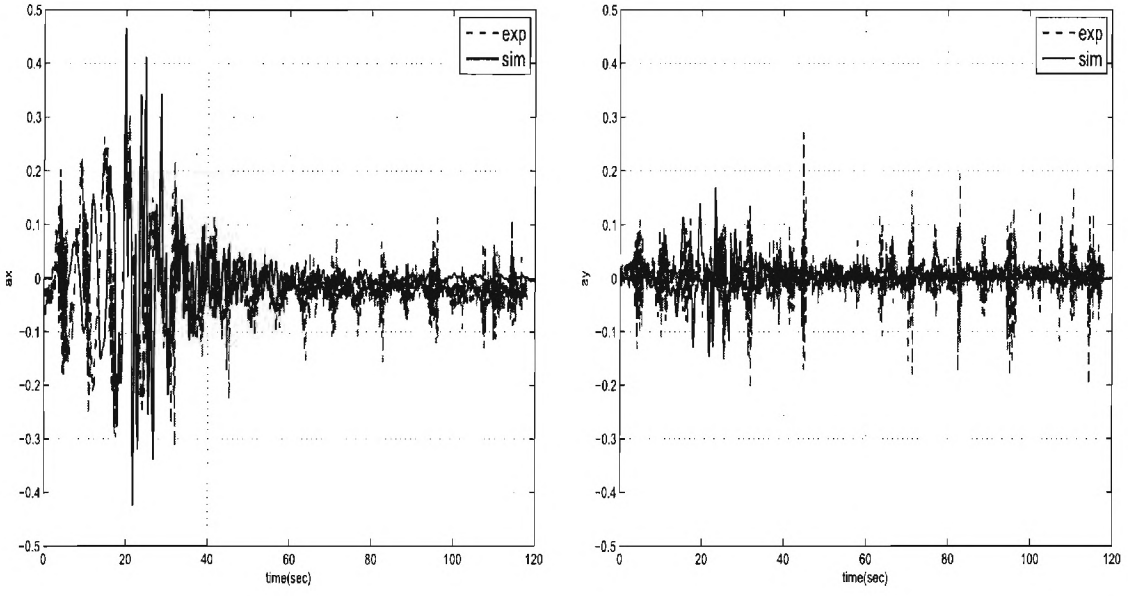

(a) a_x (b) a_y

Figure 3.17: Comparison of simulation and Experimental data when the P controller is augmented by a NN

(Solar Array Flight Experiment) boom located at NASA Marshall Space Flight Center. Whereas an attempt to design a proportional-integral controller failed due to nonlinear actuation and the lack of a sufficiently accurate structural model, the adaptive controller was successful in attenuating structural response to disturbances. Simulation studies reveal that the design of decentralized linear controllers in the presence of structural nonlinearities/couplings is a difficult task. However these same controllers can be augmented with adaptive elements that render the closed loop system performance satisfactory.

Section 4

Future Directions

While the main results in this report were obtained with the decentralized architecture in [21] due to complexity in designing a single centralized controller. Even though, recent advances in the technology of sensors and actuators allow for implementation of distributed set of inexpensive sensors and actuators for large-scales systems, most conventional control methods become proportionally complicated by the dimension of the system to be controlled and are not suitable for a large-scale system. Moreover, if the system to be controlled is uncertain, the design of a single controller for a high dimensional system becomes less feasible in most control systems. However, we note that a major obstacle associated with a concurrent controller in a large-scale system does not lie in setting up multiple communication channels among many subsystems in hardware, but in the lack of an appropriate information processing algorithm that is numerically efficient. In practice, recent advances in microprocessors and signal processing make it possible for a single system board to handle multiple channels of inputs and outputs with less power consumption compared to the past, but control design methodology for systems having distributed arrays of sensors and actuators has not kept up with this technology.

For example, let us consider the SAFE boom depicted in Figure 3.1. Besides three accelerometers and three air-jets used to obtain the results in Section 3, there are additional piezosensors, accelerometers, and piezoactuators that were not utilized. The main difficulty in utilizing these sensors and actuators was lack of modeling information. Figure 4.1 illustrates an manner in which NNs can be used to exploit the use of arrays of sensors and actuators. In model based control system design, exploitation of a large number of distributed sensors and actuators becomes a burdensome modeling task. One way a NN can be employed in the context of our present study is to use the same nominal controller for actuating the thrusters, but employ all the sensors in augmenting the nominal controller. This would extend to allowing for cross axis connections to the thrusters and to any other actuators that we may wish to employ. Each sensor output would influence the adaptive signal sent to each actuator in a different manner decided by the adaptation law. All that is required from a theoretical perspective is that the sign of the control effectiveness for each control effector be known, and that the relative degree of the regulated output be known with respect to the nominal control effectors. More generally, a NN-based adaptive controller can operate differently on each individual input of spatially distributed sensors, and the NN-outputs can be applied to each individual element in an array of spatially distributed actuators. The adaptive process can be used to decide on the weights of these interconnections. Some preliminary research towards this direction is performed in [40, 41].

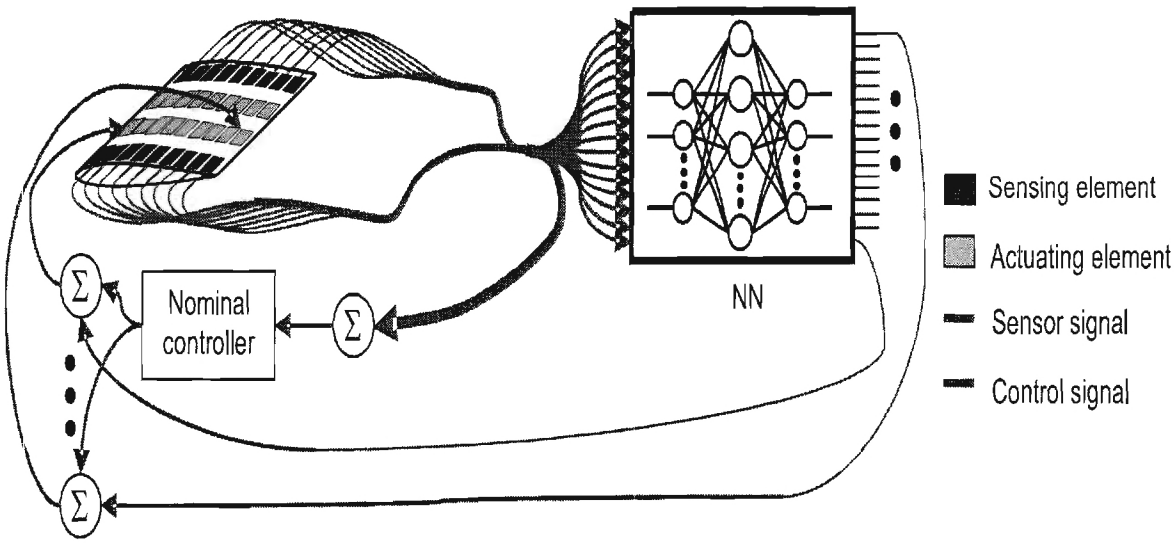

Figure 4.1: New control architecture

Bibliography

[1] McInnes, C. R., *Solar Sailing: Technology, Dynamics, and Mission Applications*, Springer-Praxis Books in Astronautical Engineering, 2004.

[2] Murphy, D. and Wie, B., "Robust Thrust Control Authority for a Scalable Sailcraft," *14th AAS/AIAA Space Flight Mechanics Conference*, AAS 04-285, Maui,HI, 2004.

[3] Wie, B., "Dynamic Modeling and Attitude Control of Solar Sail Spacecraft: Part I," *Proceedings of AIAA guidance,navigation and control conference*, AIAA 2002-4572, Monterey, CA, 2002.

[4] Wie, B., "Dynamic Modeling and Attitude Control of Solar Sail Spacecraft: Part II," *Proceedings of AIAA guidance,navigation and control conference*, AIAA 2002-4573, Monterey, CA, 2002.

[5] Wie, B., "Solar Sail Attitude Control and Dynamics, Part 1," *AIAA Journal of Guidance, Control & Dynamics*, Vol. 27, No. 4, 2004.

[6] Rotunno, M., Basso, M., Pomè, A. B., and Sallusti, M., "A Comparison of Robust Attitude Control Techniques for a Solar Sail Spacecraft," *Proceedings of AIAA guidance,navigation and control conference*, AIAA 2005-6083, San Frrancisco, CA, 2005.

[7] Smith, S. W., Song, H., Baker, J. R., and Black, J., "Flexible Models for Solar Sail Control," *46th AIAA/ASME/ASCE/AHS/ASC Structures, Structural Dynamics and Materials Conference*, AIAA 2005-1801, Austin, TX, 2005.

[8] Gorinevsky, D., Hyde, T., and Cabuz, C., "Distributed Localized Shape Control of Gossamer Space Structures," *Proceedings of AIAA/ASME/ASCE/AHS/ASC Structures, Structural Dynamics, and Materials Conference*, AIAA 2001-1197, Seattle, WA, 2001.

[9] Jha, A. K. and Inman, D. J., "Sliding Mode Control of a Gossamer Structure Using Smart Materials," *Journal of Vibration and Control*, Vol. 10, 2004, pp. 1199–1220.

[10] Ruggiero, E. J. and Inman, D. J., "Gossamer Spacecraft: Recent Trends in Design, Analysis, Experimentation, and Control," *Journal of Spacecraft and Rockets*, Vol. 43, No. 1, 2006, pp. 10–24.

[11] Sleight, D. W., Michii, Y., Lichodziejewski, D., and Derbès, B., "Structural Analysis of an Inflation-deployed Solar Sail with Experimental Validation," *41st AIAA/ASME/SAE/ASEE Joing Propulsion Conference*, AIAA 2005-3727, Tucson, AZ, 2005.

[12] Hornik, N., Stinchcombe, M., and White, H., "Multilayer feedforward networks are universal approximators," *Neural Networks*, Vol. 2, 1989, pp. 359–366.

[13] Ge, S., Lee, T., and Harris, C., *Adaptive Neural Network Control of Robotic Manipulators*, World Scientific, 1998.

[14] Lewis, F., Jagannathan, S., and Yeşildirek, A., *Neural Network Control of Robot Manipulators and Nonlinear Systems*, Taylor & Francis, 1999.

[15] Spooner, J. T., Maggiore, M., Ordóñez, R., and Passino, K. M., *Stable Adaptive Control and Estimation for Nonlinear Systems- Neural and Fuzzy Approximator Techniques*, John Wiley & Sons, New York, NY, 2002.

[16] Lavretsky, E., Hovakimyan, N., and Calise, A., "Upper Bounds for Approximation of Continuous-Time Dynamics Using Delayed Outputs and Feedforward Neural Networks," *IEEE Transactions on Automatic Control*, Vol. 48, No. 9, 2003, pp. 1606–1610.

[17] Kim, N., Calise, A. J., Hovakimyan, N., Prasad, J., and Corban, J. E., "Adaptive Output Feedback for High-Bandwidth Flight Control," *AIAA Journal of Guidance, Control & Dynamics*, Vol. 25, No. 6, 2002, pp. 993–1002.

[18] Calise, A., Yang, B.-J., and Craig, J., "An Augmenting Adaptive Approach to Control of Flexible Systems," *AIAA Journal of Guidance, Control & Dynamics*, Vol. 27, No. 3, 2004, pp. 387–396.

[19] Yang, B.-J., Hovakimyan, N., Calise, A., and Craig, J., "Experimental Validation of an Augmenting Approach to Adaptive Control of Uncertain Nonlinear Systems," *Proceedings of AIAA guidance,navigation and control conference*, AIAA-2003-5715, Austin, TX, 2003, (Submitted to IEEE Transactions on Control System Technology, 2006).

[20] Yang, B.-J., Calise, A., and Craig, J., "Adaptive Output Feedback Control of a Flexible Base Manipulator," *Proceedings of AIAA guidance,navigation and control conference*, AIAA-2004-5322, Providence, RI, August 2004, (Accepted for publication in AIAA Journal of Guidance, Control & Dynamics, 2007).

[21] Hovakimyan, N., Lavretsky, E., Yang, B.-J., and Calise, A., "Coordinated Decentralized Adaptive Output Feedback for Control of Interconnected Systems," Vol. 16, No. 1, 2005, pp. 185–194.

[22] Graybeal, N. and Craig, J. I., "Deployment Modeling of Solar Sail Structures," *Proceedings of AIAA guidance,navigation and control conference*, AIAA-2006-6336, Keystone, CO, August 2006.

[23] Marino, R. and Tomei, P., *Nonlinear Control Design: Geometric, Adaptive, & Robust*, Prentice Hall, New Jersey, 1995.

[24] Ioannou, P. and Sun, J., *Robust Adaptive Control*, Prentice-Hall, Englewood Cliffs, NJ, 1996.

[25] Hovakimyan, N., Yang, B.-J., and Calise, A. J., "Adaptive Output Feedback Control Methodology Applicable to Non-Minimum Phase Nonlinear Systems," *Automatica*, Vol. 42, No. 4, April 2006, pp. 513–522.

[26] Hovakimyan, N., Yang, B.-J., and Calise, A., "An Adaptive Output Feedback Control Methodology for Non-Minimum Phase Systems," *Proceedings of Conference on Decision and Control*, Las Vegas, NV, 2002, pp. 949–954.

[27] Kutay, A. T., Fowler, J. M., Calise, A. J., and D'Andrea, R., "Distributed Adaptive Output Feedback Control Design and Application to a Formation Flight Experiment," *Proceedings of AIAA guidance,navigation and control conference*, Aug. 2005.

[28] Calise, A., Hovakimyan, N., and Idan, M., "Adaptive Output Feedback Control of Nonlinear Systems using Neural Networks," *Automatica*, Vol. 37, No. 8, 2001, pp. 1201–1211.

[29] Hovakimyan, N., Nardi, F., Kim, N., and Calise, A., "Adaptive Output Feedback Control of Uncertain Systems using Single Hidden Layer Neural Networks," *IEEE Transactions on Neural Networks*, Vol. 13, No. 6, 2002.

[30] Gorney, D., Blake, J., Koons, H., Schulz, M., Vampola, A., and Walterscheid, R., "The Space Environment and Survivability," *Space Mission Analysis and Design*, edited by W. J. Larson and J. R. Wertz, Microcosm, Inc. and Kluwer Academic Publishers, 2nd ed., 1992.

[31] Hallauer, W., Lamberson, S., and Baer, C., "Active Vibration Damping of a Planar Truss Using Air-jet Thrusters," *Experimental Mechanics*, Vol. 31, No. 3, 1991, pp. 189–196.

[32] Casella, F., Locatelli, A., and Schiavoni, N., "Nonlinear controllers for vibration suppression in a large flexible structure," *Control Engineering Practice*, Vol. 4, No. 6, 1996, pp. 791–806.

[33] Allen, M., Bernelli-Zazzera, F., and Scattolini, R., "Sliding mode control of a large flexible space structure," *Control Engineering Practice*, Vol. 8, No. 8, 2000, pp. 861–871.

[34] Casella, F., Locatelli, A., and Schiavoni, N., "Modelling and control for vibration suppression in a large flexible structure with jet thrusters and piezoactuators," *IEEE Transactions on Control Systems Technology*, Vol. 10, No. 4, 2002, pp. 589–599.

[35] Adetona, O., Keel, L., Oakley, J., Kappus, K., Whorton, M., Kim, Y., and Rakoczy, J., "Model Correlation Study of a Retractable Boom for a Solar Sail Spacecraft," *53th JANNAF*, Monterey, CA, Dec. 5-9 2005, pp. 2442–2447.

[36] Whorton, M. S., *High Performance, Robust Control of Flexible Space Structures*, Ph.D. thesis, Georgia Institute of Technology, School of Aerospace Engineering, Atlanta, GA 30332, aug 1997.

[37] Analog Devices, Inc., www.analog.com, *Small and Thin $\pm 5g$ Accelerometer-ADXL320*, rev.0 ed., 2004.

[38] Clippard Instrument Laboratory, Inc., www.clippard.com, *EVP Series Proportional Control Valves*, Oct. 2003.

[39] Balas, M. J., "Direct Velocity Feedback Control of Large Space Structures," *AIAA Journal of Guidance, Control & Dynamics*, Vol. 2, No. 3, May-June 1979, pp. 252–253.

[40] Yang, B. J., Calise, A. J., Craig, J. I., and Kim, K., "Centralized Adaptive Control of a Complex Flexible System," *AIAA Guidance, Navgation, and Control Conference*, AIAA-2007-6686, Hilton Head, SC, 2007.

[41] Yang, B.-J., Calise, A. J., Craig, J. I., and Kim, K., "Adaptive Coordination of Decentralized Controllers using a Centralized Neural Network," *Proceedings of the American Control Conference*, Seattle, WA, 2008, Submitted.